

# Enhancing information retrieval in quantum-optical critical systems via quantum measurement backaction

Cheng Zhang,<sup>1,2</sup> Mauro Cirio,<sup>3</sup> Xin-Qi Li,<sup>1,2</sup> and Pengfei Liang<sup>1,2,\*</sup>

<sup>1</sup>*Research Center for Quantum Physics and Technologies,  
Inner Mongolia University, Hohhot 010021, China*

<sup>2</sup>*School of Physical Science and Technology, Inner Mongolia University, Hohhot 010021, China*

<sup>3</sup>*Graduate School of China Academy of Engineering Physics, Haidian District, Beijing, 100193, China*

(Dated: December 1, 2025)

Continuous monitoring of open quantum-optical systems offers a promising route towards quantum-enhanced estimation precision. In such continuous-measurement-based sensing protocols, the ultimate precision limit is dictated, through the quantum Cramér-Rao bound, by the global quantum Fisher information associated with the joint system-environment state. Reaching this limit with established continuous measurement techniques in quantum optics remains an outstanding challenge. Here we present a sensing protocol tailored for open quantum-optical sensors that exhibit dissipative criticality, enabling them to significantly narrow the gap to the ultimate precision limit. Our protocol leverages a previously unexplored interplay between the quantum criticality and the quantum measurement backaction inherent in continuous general-dyne detection. We identify a performance sweet spot, near which the ultimate precision limit can be efficiently approached. Our protocol establishes a new pathway towards quantum-enhanced precision in open quantum-optical setups and can be extended to other sensor designs featuring similar dissipative criticality.

*Introduction.*— A fundamental principle of quantum mechanics is that quantum measurement inevitably disturbs the system being observed [1]. Beyond its conceptual importance, controlling and harnessing such measurement backaction is crucial for a wide range of quantum technologies [2–13]. In quantum metrology, the quantum backaction of continuous measurements [14–16] has attracted considerable interest, proving instrumental in tasks such as generating stable spin-squeezing [3–6, 17, 18] and mitigating detrimental local dephasing noises [19, 20].

Driven quantum-optical setups [21–27] constantly emit radiation quanta into their environment, which can be continuously monitored via well-established techniques in quantum optics [14–16], e.g., photon counting, homodyne, and heterodyne detection. As a result, they serve as ideal platforms for implementing sensing protocols based on continuous measurement [28–31]. The ultimate precision achievable by such protocols is dictated, through the quantum Cramér-Rao bound (QCRB), by the global quantum Fisher information (QFI) [32–34] which quantifies the distinguishability of the underlying joint system-environment state. However, temporal correlations between the radiation quanta generally prevent saturation of this bound through conventional time-local continuous measurements. To address this challenge, Yang *et al.* recently proposed a sensor-quantum-decoder serial architecture capable of converting the correlated output field of the sensor into an uncorrelated field at the decoder [34]. Despite this important progress, there remains a pressing need for alternative approaches that can improve precision towards the QCRB in open quan-

tum sensors under realistic continuous measurement conditions.

In this work, we show that quantum measurement backaction can be exploited to narrow this gap in open quantum-optical sensors featuring dissipative critical points (CPs). Focusing on the open Kerr parametric oscillator (KPO) [35–40] subject to continuous general-dyne (or Gaussian) measurement [15, 41–45], which contains homodyne and heterodyne as special cases, we report two key findings. First, when the oscillator evades measurement backaction, such that only the quadrature irrelevant to criticality is perturbed, special CPs emerge at which quantum criticality is preserved in the conditional dynamics. Second, the presence of such backaction-evading CPs leads to a significant enhancement of the continuous-monitoring Fisher information (FI) [19, 44] in their vicinity. Based on this enhancement, we design an optimization strategy that enables close approach to the QCRB. We also characterize the performance of this strategy and analyze the impact of detection inefficiency.

*Setup.*—We consider estimating the frequency  $\omega$  of the open KPO, described by the Hamiltonian

$$H_\omega = \omega a^\dagger a + \frac{\epsilon}{2}(a^{\dagger 2} + a^2) + \chi a^{\dagger 2} a^2, \quad (1)$$

where  $\epsilon$  is the two-photon driving amplitude and  $\chi$  denotes the Kerr nonlinearity. The emission field is continuously monitored via general-dyne detection [15, 41–45], which measures two conjugate field quadratures at each time with different uncertainties. Formally, this corresponds to projecting the emission field onto a displaced squeezed-vacuum state characterized by the covariance matrix  $\sigma_m = (\mathbf{R}_\varphi^\top \sigma_0 \mathbf{R}_\varphi + 1 - \eta)/\eta$  [15, 41–44], in terms of the detection efficiency  $\eta \in [0, 1]$ , and the matrices  $\sigma_0 = \text{diag}[s, 1/s]$  and  $\mathbf{R}_\varphi = (\cos \varphi, \sin \varphi; -\sin \varphi, \cos \varphi)$ ,

\* pfliang@imu.edu.cn

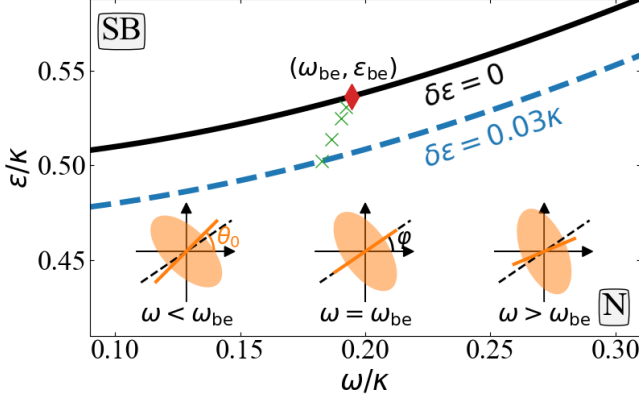


FIG. 1. Phase diagram of the open KPO without continuous general-dyne measurement. The black solid curve at  $\delta\epsilon = 0$  marks the phase boundary separating the normal phase (N) and the symmetry-broken phase (SB). The insets illustrate that under homodyne detection, a backaction-evading CP (red diamond) emerges at  $(\omega_{be}, \epsilon_{be})$  (given by Eq. (5)), when the squeezing angle  $\theta_0$  of the unconditional steady-state in the normal phase match the angle  $\varphi$  (here  $\varphi = 0.6$ ). The green crosses are described in Fig. 2.

respectively parametrized by the squeezing degree  $s \in [0, 1]$  and the squeezing angle  $\varphi \in [-\pi, \pi]$ .

Under this general-dyne monitoring, the conditional state  $\rho_c$  of the KPO evolves according to the stochastic master equation (SME) [15]

$$d\rho_c = -i[H_\omega, \rho_c]dt + \kappa\mathcal{D}[a]\rho_c dt + \sqrt{\eta\kappa}(d\mathbf{w}^\top \mathbf{B} \Delta \mathbf{a} \rho_c + \rho_c \Delta \mathbf{a}^\dagger \mathbf{B} d\mathbf{w}), \quad (2)$$

where  $\kappa$  is the photon loss rate,  $\Delta \mathbf{a} = (a - \langle a \rangle_c, i(a^\dagger - \langle a^\dagger \rangle_c))^\top$  with  $\langle \cdot \rangle_c = \text{Tr}[\cdot \rho_c]$ . Here, the vector  $d\mathbf{w} = (dw_1, dw_2)^\top$  consists of two independent Wiener increments  $dw_1$  and  $dw_2$  satisfying  $\mathbb{E}[d\mathbf{w}] = 0$  and  $\mathbb{E}[d\mathbf{w}d\mathbf{w}^\top] = \mathbf{I}dt$ , in terms of the  $2 \times 2$  identity matrix  $\mathbf{I}$ . The matrix  $\mathbf{B} = [(\mathbf{I} + \boldsymbol{\sigma}_m)/\eta]^{-1/2}$  characterizes the dynamics of the recorded photocurrent as  $dy_t = \sqrt{2\kappa\eta}\mathbf{B}rdt + d\mathbf{w}$  with mean vector  $\mathbf{r} = (\langle x \rangle_c, \langle p \rangle_c)^\top$ . Note that, in the limit  $s \rightarrow 0$  and  $s \rightarrow 1$ , Eq. (2) describes the conditional dynamics under homodyne and heterodyne detection, respectively.

In the absence of continuous monitoring ( $\eta = 0$ ), the open KPO exhibits two different kinds of phase transitions in the scaling limit  $\chi \rightarrow 0$ , depending on the sign of  $\omega$  [35–40]. Specifically, for  $\omega > 0$  ( $\omega < 0$ ), the system undergoes a continuous (first-order) phase transition from the normal phase to the  $\mathbb{Z}_2$  symmetry-broken phase. The phase boundary for the continuous phase transition is given by  $\epsilon_c = \sqrt{\omega^2 + \kappa^2/4}$  [46, 47]. Hereafter we denote by  $\delta\epsilon = \epsilon_c - \epsilon$  the boundary proximity. Since quantum criticality plays a central role in this work, we focus on estimating positive frequency  $\omega > 0$ , and operate the sensor in the normal phase ( $\delta\epsilon > 0$ ).

In the normal phase of the unconditional model, the scaling limit is attained by setting  $\chi = 0$  in the Kerr Hamiltonian (1), which remains valid in the conditional

case with  $\eta > 0$ . In this limit, the conditional state  $\rho_c$  retains its Gaussian character for any Gaussian initial state. We denote by  $\Sigma_O = 2(\langle O^2 \rangle_c - \langle O \rangle_c^2)$  the variance of the operator  $O$ , and  $\Sigma_{O_1 O_2} = \langle \{O_1, O_2\} \rangle_c - 2\langle O_1 \rangle_c \langle O_2 \rangle_c$  the covariance between the operators  $O_1$  and  $O_2$ . The conditional state  $\rho_c$  is then fully characterized by its mean vector  $\mathbf{r}$  and its covariance matrix  $\boldsymbol{\Sigma} = (\Sigma_x, \Sigma_{xp}; \Sigma_{xp}, \Sigma_p)$ , which obey the following differential equations [15, 44]

$$d\mathbf{r} = \mathbf{A}d\mathbf{r} + \sqrt{\frac{\eta\kappa}{2}}(\boldsymbol{\Sigma} - \mathbf{I})\mathbf{B}d\mathbf{w}, \quad (3a)$$

$$\frac{d\boldsymbol{\Sigma}}{dt} = \mathbf{A}\boldsymbol{\Sigma} + \boldsymbol{\Sigma}\mathbf{A}^\top + \mathbf{D} - \eta\kappa(\boldsymbol{\Sigma} - \mathbf{I})\mathbf{B}^2(\boldsymbol{\Sigma} - \mathbf{I}), \quad (3b)$$

with the coefficient matrices  $\mathbf{A} = (-\kappa/2, \omega - \epsilon; -\omega - \epsilon, -\kappa/2)$  and  $\mathbf{D} = \text{diag}(\kappa, \kappa)$ . In Sec. I of the Supplemental Material (SM) [48], we provide details for deriving Eq. (3) from the SME (2).

The backaction term in Eq. (3b), i. e.,  $-\eta\kappa(\boldsymbol{\Sigma} - \mathbf{I})\mathbf{B}^2(\boldsymbol{\Sigma} - \mathbf{I})$ , is negative semi-definite, indicating that general-dyne measurements generally suppress fluctuations (encoded in  $\boldsymbol{\Sigma}$ ) in the conditional state. Given that quantum criticality is characterized by the divergence of fluctuations, a natural question arises: does quantum criticality persist in the conditional state under continuous general-dyne monitoring? In what follows, we provide an affirmative answer to this question.

*Backaction-evading critical points.*— As sketched in the insets of Fig. 1, we first present a perturbation analysis of the steady-state covariance  $\boldsymbol{\Sigma}_{ss}$ , valid for small efficiency  $\eta \ll 1$ . To begin our analysis, we consider that, in the normal phase, the unconditional steady-state  $\rho_0^{ss}$ , i. e., the stationary solution to Eq. (2) for  $\eta = 0$ , is simply a squeezed state with squeezing angle  $\theta_0 = \tan^{-1}(\kappa/2\omega)/2$ . Its covariance matrix  $\boldsymbol{\Sigma}_{ss}^{(0)}$ , determined by the equation  $\mathbf{A}\boldsymbol{\Sigma}_{ss}^{(0)} + \boldsymbol{\Sigma}_{ss}^{(0)}\mathbf{A}^\top + \mathbf{D} = 0$ , admits the analytical form  $\boldsymbol{\Sigma}_{ss}^{(0)} = (\epsilon_c^2 - \omega\epsilon, -\kappa\epsilon/2; -\kappa\epsilon/2, \epsilon_c^2 + \omega\epsilon)/(\epsilon_c^2 - \epsilon^2)$  [46, 47]. As a result, the quadratures  $x_{\theta_0} = x \cos \theta_0 + p \sin \theta_0$  and  $p_{\theta_0} = -x \sin \theta_0 + p \cos \theta_0$  exhibit squeezing and antisqueezing, respectively. Their covariance matrix  $\bar{\boldsymbol{\Sigma}}_{ss}^{(0)}$  can be obtained via the rotation  $\bar{\boldsymbol{\Sigma}}_{ss}^{(0)} = \mathbf{R}_{\theta_0}\boldsymbol{\Sigma}_{ss}^{(0)}\mathbf{R}_{\theta_0}^\top$ , where  $\mathbf{R}_{\theta_0} = (\cos \theta_0, \sin \theta_0; -\sin \theta_0, \cos \theta_0)$  is the corresponding rotation matrix, and takes the diagonal form  $\bar{\boldsymbol{\Sigma}}_{ss}^{(0)} = \text{diag}[\epsilon_c/(\epsilon_c + \epsilon), \epsilon_c/(\epsilon_c - \epsilon)]$ . Importantly, as the critical point is approached,  $\epsilon \rightarrow \epsilon_c$ , the quadrature  $p_{\theta_0}$  becomes infinitely antisqueezed, an essential prerequisite for the emergence of quantum criticality.

We now expand the rotated covariance  $\bar{\boldsymbol{\Sigma}}_{ss} = \bar{\boldsymbol{\Sigma}}_{ss}^{(0)} + \eta\bar{\boldsymbol{\Sigma}}_{ss}^{(1)} + \mathcal{O}(\eta^2)$ , where  $\bar{\boldsymbol{\Sigma}}_{ss} = \mathbf{R}_{\theta_0}\boldsymbol{\Sigma}_{ss}\mathbf{R}_{\theta_0}^\top$  and  $\bar{\boldsymbol{\Sigma}}_{ss}^{(1)}$  is the first-order correction. Substituting this expansion into Eq. (3b), one can obtain  $\bar{\boldsymbol{\Sigma}}_{ss}^{(1)}$  by solving the following algebraic Riccati equation  $\bar{\mathbf{A}}\bar{\boldsymbol{\Sigma}}_{ss}^{(1)} + \bar{\boldsymbol{\Sigma}}_{ss}^{(1)}\bar{\mathbf{A}}^\top = \kappa\mathcal{B}[\bar{\boldsymbol{\Sigma}}_{ss}^{(0)}, \bar{\mathbf{B}}]$ , where  $\bar{\mathbf{A}} = \mathbf{R}_{\theta_0}\mathbf{A}\mathbf{R}_{\theta_0}^\top$ ,  $\bar{\mathbf{B}} = \mathbf{R}_{\theta_0}\mathbf{B}\mathbf{R}_{\theta_0}^\top$  and  $\mathcal{B}[\bar{\boldsymbol{\Sigma}}_{ss}^{(0)}, \bar{\mathbf{B}}] = (\bar{\boldsymbol{\Sigma}}_{ss}^{(0)} - \mathbf{I})\bar{\mathbf{B}}^2(\bar{\boldsymbol{\Sigma}}_{ss}^{(0)} - \mathbf{I})$ . A particularly interesting case is the homodyne detection ( $s = 0$ ), where  $\mathcal{B}[\bar{\boldsymbol{\Sigma}}_{ss}^{(0)}, \bar{\mathbf{B}}]$  can

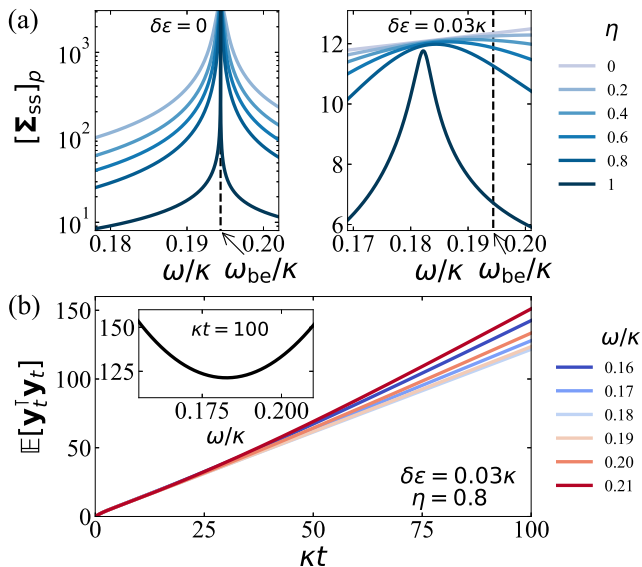


FIG. 2. (a) Covariance component  $[\Sigma_{ss}]_p$  evaluated (left) on the phase boundary  $\delta\epsilon = 0$  and (right) near the phase boundary  $\delta\epsilon = 0.03\kappa$  for different detection efficiency  $\eta$ . Vertical dashed lines indicate the location of the backaction-evading CP for  $\varphi = 0.6$ . Note that, the curve corresponding to  $\eta = 0$  is not shown in the left panel as  $[\Sigma_{ss}]_p$  diverges on the phase boundary in the unconditional case. (b) Time evolution of the variance of the integrated photocurrent  $\mathbb{E}[\mathbf{y}_t^T \mathbf{y}_t]$  for selected  $\omega$  along  $\delta\epsilon = 0.03\kappa$ . Inset shows the current profile at  $\kappa t = 100$ . The minimum location  $\omega \approx 0.1825\kappa$  in this case, alongside those for  $\delta\epsilon/\kappa = 0.02, 0.01, 0.005$ , are shown as green crosses in Fig. 1. All simulations correspond to homodyne detection with  $s = 0$  and  $\varphi = 0.6$ .

be written explicitly in a compact form

$$\mathcal{B}[\bar{\Sigma}_{ss}^{(0)}, \bar{\mathbf{B}}] = \begin{pmatrix} \frac{\epsilon^2 \cos^2(\theta_0 - \varphi)}{(\epsilon_c + \epsilon)^2} & \frac{\epsilon^2 \sin 2(\theta_0 - \varphi)}{2(\epsilon_c^2 - \epsilon^2)} \\ \frac{\epsilon^2 \sin 2(\theta_0 - \varphi)}{2(\epsilon_c^2 - \epsilon^2)} & \frac{\epsilon^2 \sin^2(\theta_0 - \varphi)}{(\epsilon_c - \epsilon)^2} \end{pmatrix}. \quad (4)$$

This equation reveals a backaction-evading mechanism under homodyne detection: For any  $\omega > 0$ , choosing  $\varphi = \theta_0$  yields  $\mathcal{B}[\bar{\Sigma}_{ss}^{(0)}, \bar{\mathbf{B}}] = (\epsilon^2/(\epsilon_c + \epsilon)^2, 0; 0, 0)$ , so that the measurement backaction only perturbs  $x_{\theta_0}$ , the quadrature irrelevant to the emergence of quantum criticality in the unconditional state  $\rho_0^{\text{ss}}$ . In such a situation, the first-order correction  $\bar{\Sigma}_{ss}^{(1)}$  remains finite even at the corresponding CP, therefore preserving quantum criticality in the conditional dynamics. In contrast, when  $\varphi \neq \theta_0$ , the first-order correction diverges to negative infinity at this CP, possibly suppressing criticality in the conditional state. By solving the equation  $\varphi = \theta_0$ , we find the parametrization of these backaction-evading CPs

$$(\omega_{\text{be}}, \epsilon_{\text{be}}) = \left( \frac{\kappa}{2} \cot(2\varphi), \frac{\kappa}{2 \sin(2\varphi)} \right), \quad (5)$$

where, recalling the restriction  $\omega > 0$ , we require  $\varphi \in (0, \pi/4)$  for consistency.

Numerical simulations confirm the presence of backaction-evading CPs beyond the perturbative regime. Throughout our numerical analysis, we choose the vacuum as the initial state. Fig. 2(a) (left panel) shows  $[\Sigma_{ss}]_p$  along the phase boundary  $\delta\epsilon = 0$  for different  $\eta$  at fixed  $\varphi = 0.6$ . Consistent with our perturbation analysis, critical fluctuations are strongly suppressed except at  $\omega_{\text{be}} \approx 0.194\kappa$ , where they diverge independently of the efficiency  $\eta$ . Similar behavior is observed for other covariance components  $[\Sigma_{ss}]_x, [\Sigma_{ss}]_{xp}$  (see the SM [48], Sec. II). Notably, away from the phase boundary ( $\delta\epsilon = 0.03\kappa$ , right panel), the divergence transforms into a pronounced fluctuation peak. This feature plays a critical role in shaping the long-time behavior of the FI, a point illustrated in Fig. 3(a) and explored further in a subsequent section.

These special CPs can be detected experimentally through the integrated photocurrent,  $\mathbf{y}_t = \int_0^t d\mathbf{y}_t$ . To illustrate this, we select several points along the line  $\delta\epsilon = 0.03\kappa$  and show in Fig. 2(b) the evolution of the variance of the integrated photocurrent  $\mathbb{E}[\mathbf{y}_t^T \mathbf{y}_t]$  under non-ideal homodyne detection with  $\eta = 0.8$ . In Sec. III A of the SM [48], we derive a set of deterministic differential equations to compute  $\mathbb{E}[\mathbf{y}_t^T \mathbf{y}_t]$ . Interestingly,  $\mathbb{E}[\mathbf{y}_t^T \mathbf{y}_t]$  exhibits distinct growth rates at long times. Its profile at a fixed time (e.g.,  $\kappa t = 100$ , inset) develops a characteristic minimum. As  $\delta\epsilon$  is varied to approach the phase boundary,  $\delta\epsilon \rightarrow 0$ , this minimum (marked as green crosses in Fig. 1) converges to the corresponding backaction-evading CP. This convergence thus provides a viable experimental method for detecting backaction-evading CPs. An intuitive argument for understanding the occurrence of this minimum is provided in Sec. III C of the SM [48].

*Long-time behavior of the (quantum) Fisher information.*— With the existence of backaction-evading CPs established, let us now discuss their metrological utility in terms of the continuous-monitoring FI  $F(\varphi, s) = \int D\mathbf{y}_{\leq t} (\partial \ln p_{\text{gd}}(\mathbf{y}_{\leq t}|\omega)/\partial \omega)^2 p_{\text{gd}}(\mathbf{y}_{\leq t}|\omega)$ , where the likelihood  $p_{\text{gd}}(\mathbf{y}_{\leq t}|\omega)$  gives the probability of obtaining the photocurrent record  $\mathbf{y}_{\leq t} = \{\mathbf{y}_\tau | \tau \leq t\}$  up to time  $t$ , conditioned on the true frequency  $\omega$ . Here, we explicitly highlight the dependence of the FI on  $\varphi$  and  $s$  for later convenience.

Thanks to the Gaussianity of the open KPO in the scaling limit  $\chi \rightarrow 0$ ,  $F(\varphi, s)$  can be evaluated via the simplified formula [44]

$$F(\varphi, s) = 2\eta\kappa \int_0^t d\tau \mathbb{E} [(\partial_\omega \mathbf{r}^\top) \mathbf{B}^2 (\partial_\omega \mathbf{r})]. \quad (6)$$

This expression implies that the FI grows linearly at long times, i. e.,  $F(\varphi, s) \sim k_F t$ , with the growth rate given by  $k_F = 2\eta\kappa \lim_{t \rightarrow \infty} \mathbb{E} [(\partial_\omega \mathbf{r}^\top) \mathbf{B}^2 (\partial_\omega \mathbf{r})]$ . In Sec. IV A of the SM [48], we further derive a set of deterministic differential equations to calculate the integrand  $\mathbb{E} [(\partial_\omega \mathbf{r}^\top) \mathbf{B}^2 (\partial_\omega \mathbf{r})]$ , thereby avoiding the computationally-costly ensemble average required by Eq. (6).

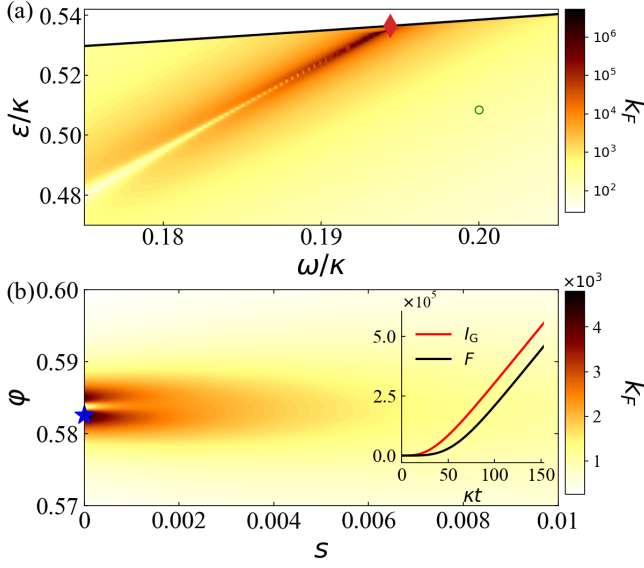


FIG. 3. (a) The long-time growth rate  $k_F$  of the FI  $F(\varphi, s)$  under homodyne detection as a function of  $\omega$  and  $\epsilon$ . The red diamond corresponds to the backaction-evading CP for  $\varphi = 0.6$ . (b) Optimization of  $k_F$  over the parameters  $\varphi$  and  $s$  for  $(\omega, \delta\epsilon) = (0.2\kappa, 0.03\kappa)$ , marked by the green circle in (a). The optimal general-dyne measurement is identified as  $(s_{\text{opt}}, \varphi_{\text{opt}}) = (0, 0.583)$  (blue star). The inset compares the FI  $F(\varphi_{\text{opt}}, s_{\text{opt}})$  under this optimal measurement and the corresponding global QFI denoted as  $I_G$ . All simulations assume ideal detection efficiency  $\eta = 1$ .

The FI  $F(\varphi, s)$  is bounded from above by the global QFI [32–34]

$$I_G = 4\partial_{\omega_1}\partial_{\omega_2}\ln\mathcal{F}(\omega_1, \omega_2)|_{\omega_1=\omega_2=\omega}, \quad (7)$$

where  $\mathcal{F}(\omega_1, \omega_2)$  denotes the quantum fidelity of the underlying joint oscillator-environment state [32]. This fidelity can be calculated as  $\mathcal{F}(\omega_1, \omega_2) = |\text{Tr}[\mu_{\omega_1, \omega_2}]|$ , where the operator  $\mu_{\omega_1, \omega_2}$  obeys the generalized master equation [32–34]

$$\frac{d\mu_{\omega_1, \omega_2}}{dt} = -i(H_{\omega_1}\mu_{\omega_1, \omega_2} - \mu_{\omega_1, \omega_2}H_{\omega_2}) + \kappa\mathcal{D}[a]\mu_{\omega_1, \omega_2}. \quad (8)$$

In Sec. IV B of the SM [48], we rigorously use Eq. (8) to prove that, in the scaling limit  $\chi \rightarrow 0$ , the global QFI  $I_G$  also grows linearly at long times as  $I_G \sim k_G t$ , with  $k_G$  its growth rate. An analytical expression of  $k_G$  is also derived.

*Enhancement of information retrieval.*— We now demonstrate that the long-time growth of  $F(\varphi, s)$ , as quantified by the rate  $k_F$ , is strongly enhanced in the vicinity of backaction-evading CPs. In Fig. 3(a), we plot the landscape of  $k_F$  near a fixed backaction-evading CP (red diamond) under ideal homodyne detection, i.e.,  $s = 0$  and  $\eta = 1$ . This CP corresponds to  $\varphi = 0.6$  in Eq. (5). A notable feature is the double-peak structure around this CP, which ultimately merges at the CP itself. This pattern can be intuitively understood from the

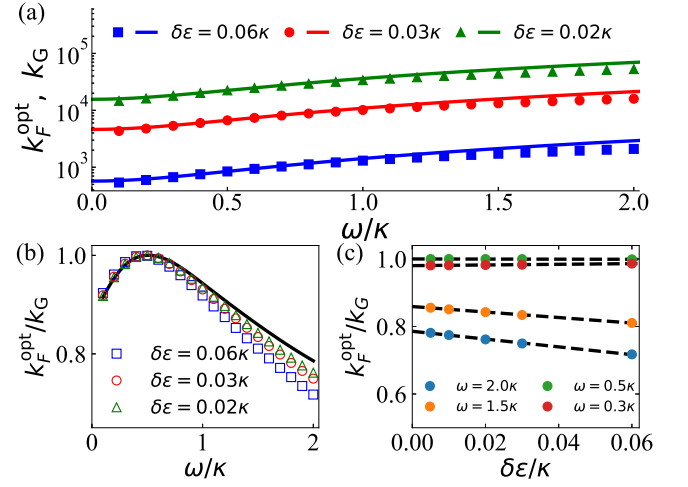


FIG. 4. (a) The growth rates  $k_F^{\text{opt}}$  (symbols) and  $k_G$  (lines) and (b) their ratio  $k_F^{\text{opt}}/k_G$  as functions of  $\omega$  for  $\delta\epsilon/\kappa = 0.06$ ,  $0.03$  and  $0.02$ . The solid curve in (b) represents the linear extrapolation of  $k_F^{\text{opt}}/k_G$  to the phase boundary  $\delta\epsilon = 0$ . (c) Four selected examples illustrating the linear extrapolation of  $k_F^{\text{opt}}/k_G$ . All simulations assume ideal detection efficiency  $\eta = 1$ .

fluctuation peak shown in the right panel of Fig. 2(a): the steep slopes on both sides of the peak make the fluctuations more sensitive to variations in frequency, giving rise to the observed characteristic structure of  $k_F$ .

Motivated by this enhancement, we develop a strategy to optimize general-dyne measurements, that is, by tuning the angle  $\varphi$  to adjust the location of backaction-evading CPs. Specifically, for fixed  $\omega$  and  $\epsilon$ , we maximize  $k_F$  over  $\varphi$  and  $s$ , and define the optimal measurement as  $(\varphi_{\text{opt}}, s_{\text{opt}}) = \text{argmax}_{\varphi, s} k_F$  with  $k_F^{\text{opt}}$  denoting the corresponding optimal growth rate. This optimization is illustrated in Fig. 3(b) for  $(\omega, \delta\epsilon) = (0.2\kappa, 0.03\kappa)$  and ideal efficiency  $\eta = 1$ . The optimal scheme is found at  $s_{\text{opt}} = 0$ , corresponding to homodyne detection, and  $\varphi_{\text{opt}} \approx 0.583$ . The inset compares the FI under this optimal measurement with the corresponding global QFI. Remarkably, their long-time growth rates nearly coincide, confirming the effectiveness of our optimization strategy.

To further assess the performance of this strategy, we plot  $k_F^{\text{opt}}$  and  $k_G$  as functions of  $\omega$  in Fig. 4(a), and their ratio  $k_F^{\text{opt}}/k_G$  in Fig. 4(b). The best performance occurs at  $\omega = 0.5\kappa$  where  $k_F^{\text{opt}}/k_G = 1$ , indicating that the conditional state  $\rho_c$  becomes as informative as the full oscillator-environment state in the long-time limit, since they yield the same amount of information within unit time. Over a broad range around this sweet spot,  $k_F^{\text{opt}}$  remains strongly enhanced. Approaching the phase boundary  $\delta\epsilon \rightarrow 0$ , the ratio  $k_F^{\text{opt}}/k_G$  converges to the black solid line in Fig. 4(b), obtained via linear extrapolation of  $k_F^{\text{opt}}/k_G$  to  $\delta\epsilon = 0$ , as illustrated in Fig. 4(c) for selected values of  $\omega$ .

*Non-ideal detection  $\eta < 1$ .*— Finally, we examine the



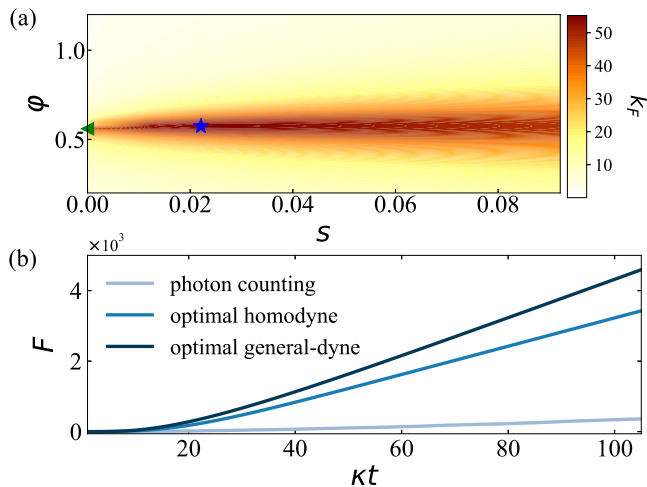


FIG. 5. (a) Optimization of  $k_F$  for  $(\omega, \delta\epsilon) = (0.2\kappa, 0.03\kappa)$  with non-ideal detection efficiency  $\eta = 0.8$ . The optimal general-dyne measurement occurs at  $(s_{\text{opt}}, \varphi_{\text{opt}}) = (0.022, 0.574)$  (blue star) while the optimal homodyne is achieved  $(s, \varphi) = (0, 0.56)$  (green triangle). (b) Time evolution of the corresponding FI for the optimal homodyne and general-dyne detection schemes in (a), compared with photon counting with the same efficiency.

performance of our strategy under non-ideal detection conditions. Fig. 5(a) shows the optimization of  $k_F$  for  $(\omega, \delta\epsilon) = (0.2\kappa, 0.03\kappa)$  and  $\eta = 0.8$ . The optimum is achieved at  $(s_{\text{opt}}, \varphi_{\text{opt}}) = (0.022, 0.574)$ . Compared to the ideal case  $\eta = 1$  in Fig. 3(b), the magnitude of  $k_F^{\text{opt}}$  is significantly reduced. Nevertheless, despite this reduction in overall performance, a clear enhancement of  $k_F$  is still observed.

To further emphasize the advantage of our approach, Fig. 5(b) compares the FI obtained from the optimal general-dyne and homodyne measurements with that from photon counting, all under the same detection efficiency. We note that photon counting was used in Ref. [33] to demonstrate the advantageous resource scal-

ing at dissipative critical points enabled by continuous monitoring. Notably, both our optimized homodyne and general-dyne schemes substantially outperform photon counting.

*Conclusions and outlook.*— In summary, we have introduced a sensing protocol to improve the frequency estimation precision towards the QCRB in the open KPO sensor. The novelty of our approach lies in the intentional use of the measurement backaction from continuous general-dyne detection to yield special CPs that effectively evade the backaction. We have demonstrated significant enhancement of the FI achieved near these CPs, and developed an optimization strategy based on their active control to approach the QCRB. As an additional outcome, our results offer a practical route to detect dissipative criticality in quantum-optical setups.

This protocol can be further advanced by addressing two primary limitations: its early-time inefficiency, reflected in the lag of the FI behind the global QFI during transient dynamics, see the inset of Fig. 3(b), and its degraded performance under non-ideal monitoring. Incorporating feedback control [14] may help mitigate both limitations.

The protocol developed here can be readily extended to other sensor designs that exhibit similar dissipative criticality. Representative examples include the quantum Rabi model [49, 50], coupled resonators [51], and fully connected systems such as the Dicke [52] and the Lipkin-Meshkov-Glick [53] models. Interesting future directions could be exploring the performance of advanced estimation techniques (e.g., maximum likelihood estimation [54], extended Kalman filtering [55–57], and neural networks [31, 58]), incorporating the formalism of past quantum state [59, 60], and implementing the tracking of time-varying signals [30, 61].

*Acknowledgements.*— C.Z. acknowledges support from CPSF (Grants No. 2025M1773419). M.C. acknowledges support from NSFC (Grant No. 12088101) and NSAF (Grant No. U2330401).

- 
- [1] M. A. Nielsen and I. L. Chuang, *Quantum Computation and Quantum Information: 10th Anniversary Edition* (Cambridge University Press, 2010).
  - [2] R. Raussendorf and H. J. Briegel, A one-way quantum computer, *Phys. Rev. Lett.* **86**, 5188 (2001).
  - [3] J. Geremia, J. K. Stockton, A. C. Doherty, and H. Mabuchi, Quantum Kalman filtering and the Heisenberg limit in atomic magnetometry, *Phys. Rev. Lett.* **91**, 250801 (2003).
  - [4] K. Mølmer and L. B. Madsen, Estimation of a classical parameter with Gaussian probes: Magnetometry with collective atomic spins, *Phys. Rev. A* **70**, 052102 (2004).
  - [5] L. B. Madsen and K. Mølmer, Spin squeezing and precision probing with light and samples of atoms in the Gaussian description, *Phys. Rev. A* **70**, 052324 (2004).
  - [6] J. K. Stockton, J. M. Geremia, A. C. Doherty, and H. Mabuchi, Robust quantum parameter estimation: Coherent magnetometry with feedback, *Phys. Rev. A* **69**, 032109 (2004).
  - [7] P. Walther, K. J. Resch, T. Rudolph, E. Schenck, H. Weinfurter, V. Vedral, M. Aspelmeyer, and A. Zeilinger, Experimental one-way quantum computing, *Nature* **434**, 169 (2005).
  - [8] A. M. Childs, D. W. Leung, and M. A. Nielsen, Unified derivations of measurement-based schemes for quantum computation, *Phys. Rev. A* **71**, 032318 (2005).
  - [9] S. Benjamin, B. Lovett, and J. Smith, Prospects for measurement-based quantum computing with solid state spins, *Laser & Photonics Reviews* **3**, 556 (2009).
  - [10] A. Kolli, B. W. Lovett, S. C. Benjamin, and T. M. Stace, Measurement-based approach to entanglement generation in coupled quantum dots, *Phys. Rev. B* **79**, 035315 (2009).

- (2009).
- [11] M. S. Blok, C. Bonato, M. L. Markham, D. J. Twitchen, V. V. Dobrovitski, and R. Hanson, Manipulating a qubit through the backaction of sequential partial measurements and real-time feedback, *Nature Physics* **10**, 189 (2014).
- [12] E. I. Rosenthal, C. M. F. Schneider, M. Malnou, Z. Zhao, F. Leditzky, B. J. Chapman, W. Wustmann, X. Ma, D. A. Palken, M. F. Zanner, L. R. Vale, G. C. Hilton, J. Gao, G. Smith, G. Kirchmair, and K. W. Lehnert, Efficient and low-backaction quantum measurement using a chip-scale detector, *Phys. Rev. Lett.* **126**, 090503 (2021).
- [13] T.-C. Wei, *Measurement-based quantum computation* (2021).
- [14] H. M. Wiseman and G. J. Milburn, *Quantum Measurement and Control* (Cambridge University Press, 2009).
- [15] A. Serafini, *Quantum Continuous Variables: A Primer of Theoretical Methods* (CRC Press, 2017).
- [16] F. Albarelli and M. G. Genoni, A pedagogical introduction to continuously monitored quantum systems and measurement-based feedback, *Physics Letters A* **494**, 129260 (2024).
- [17] B. A. Chase, B. Q. Baragiola, H. L. Partner, B. D. Black, and J. M. Geremia, Magnetometry via a double-pass continuous quantum measurement of atomic spin, *Phys. Rev. A* **79**, 062107 (2009).
- [18] F. Albarelli, M. A. C. Rossi, M. G. A. Paris, and M. G. Genoni, Ultimate limits for quantum magnetometry via time-continuous measurements, *New Journal of Physics* **19**, 123011 (2017).
- [19] F. Albarelli, M. A. C. Rossi, D. Tamascelli, and M. G. Genoni, Restoring Heisenberg scaling in noisy quantum metrology by monitoring the environment, *Quantum* **2**, 110 (2018).
- [20] M. A. C. Rossi, F. Albarelli, D. Tamascelli, and M. G. Genoni, Noisy quantum metrology enhanced by continuous nondemolition measurement, *Phys. Rev. Lett.* **125**, 200505 (2020).
- [21] K. Baumann, C. Guerlin, F. Brennecke, and T. Esslinger, Dicke quantum phase transition with a superfluid gas in an optical cavity, *Nature* **464**, 1301 (2010).
- [22] O. Castaños, R. López-Peña, E. Nahmad-Achar, and J. G. Hirsch, Quantum phase transitions in the LMG model by means of quantum information concepts, *Journal of Physics: Conference Series* **387**, 012021 (2012).
- [23] H. Ritsch, P. Domokos, F. Brennecke, and T. Esslinger, Cold atoms in cavity-generated dynamical optical potentials, *Rev. Mod. Phys.* **85**, 553 (2013).
- [24] M. P. Baden, K. J. Arnold, A. L. Grimsmo, S. Parkins, and M. D. Barrett, Realization of the Dicke model using cavity-assisted Raman transitions, *Phys. Rev. Lett.* **113**, 020408 (2014).
- [25] G. Salvatori, A. Mandarino, and M. G. A. Paris, Quantum metrology in Lipkin-Meshkov-Glick critical systems, *Phys. Rev. A* **90**, 022111 (2014).
- [26] S. R. K. Rodriguez, W. Casteels, F. Storme, N. Carlon Zambon, I. Sagnes, L. Le Gratiet, E. Galopin, A. Lemaître, A. Amo, C. Ciuti, and J. Bloch, Probing a dissipative phase transition via dynamical optical hysteresis, *Phys. Rev. Lett.* **118**, 247402 (2017).
- [27] M.-J. Hwang, P. Rabl, and M. B. Plenio, Dissipative phase transition in the open quantum Rabi model, *Phys. Rev. A* **97**, 013825 (2018).
- [28] S. Gammelmark and K. Mølmer, Bayesian parameter inference from continuously monitored quantum systems, *Phys. Rev. A* **87**, 032115 (2013).
- [29] A. H. Kiilerich and K. Mølmer, Estimation of atomic interaction parameters by photon counting, *Phys. Rev. A* **89**, 052110 (2014).
- [30] C. Zhang and K. Mølmer, Estimating a fluctuating magnetic field with a continuously monitored atomic ensemble, *Phys. Rev. A* **102**, 063716 (2020).
- [31] M. Khanahmadi and K. Mølmer, Time-dependent atomic magnetometry with a recurrent neural network, *Phys. Rev. A* **103**, 032406 (2021).
- [32] S. Gammelmark and K. Mølmer, Fisher information and the quantum Cramér-Rao sensitivity limit of continuous measurements, *Phys. Rev. Lett.* **112**, 170401 (2014).
- [33] T. Ilias, D. Yang, S. F. Huelga, and M. B. Plenio, Criticality-enhanced quantum sensing via continuous measurement, *PRX Quantum* **3**, 010354 (2022).
- [34] D. Yang, S. F. Huelga, and M. B. Plenio, Efficient information retrieval for sensing via continuous measurement, *Phys. Rev. X* **13**, 031012 (2023).
- [35] H. M. Gibbs, S. L. McCall, and T. N. C. Venkatesan, Differential gain and bistability using a sodium-filled Fabry-Perot interferometer, *Phys. Rev. Lett.* **36**, 1135 (1976).
- [36] P. D. Drummond and D. F. Walls, Quantum theory of optical bistability. i. nonlinear polarisability model, *Journal of Physics A: Mathematical and General* **13**, 725 (1980).
- [37] N. Bartolo, F. Minganti, W. Casteels, and C. Ciuti, Exact steady state of a Kerr resonator with one- and two-photon driving and dissipation: Controllable Wigner-function multimodality and dissipative phase transitions, *Phys. Rev. A* **94**, 033841 (2016).
- [38] W. Casteels, R. Fazio, and C. Ciuti, Critical dynamical properties of a first-order dissipative phase transition, *Phys. Rev. A* **95**, 012128 (2017).
- [39] F. Minganti, A. Biella, N. Bartolo, and C. Ciuti, Spectral theory of Liouvillians for dissipative phase transitions, *Phys. Rev. A* **98**, 042118 (2018).
- [40] M. J. Kewming, M. T. Mitchison, and G. T. Landi, Diverging current fluctuations in critical Kerr resonators, *Phys. Rev. A* **106**, 033707 (2022).
- [41] H. Wiseman and L. Diósi, Complete parameterization, and invariance, of diffusive quantum trajectories for Markovian open systems, *Chemical Physics* **268**, 91 (2001).
- [42] H. M. Wiseman and A. C. Doherty, Optimal unravellings for feedback control in linear quantum systems, *Phys. Rev. Lett.* **94**, 070405 (2005).
- [43] M. G. Genoni, L. Lami, and A. Serafini, Conditional and unconditional Gaussian quantum dynamics, *Contemporary Physics* **57**, 331 (2016).
- [44] M. G. Genoni, Cramér-Rao bound for time-continuous measurements in linear Gaussian quantum systems, *Phys. Rev. A* **95**, 012116 (2017).
- [45] R. Yanagimoto, R. Nehra, R. Hamerly, E. Ng, A. Marandi, and H. Mabuchi, Quantum nondemolition measurements with optical parametric amplifiers for ultrafast universal quantum information processing, *PRX Quantum* **4**, 010333 (2023).
- [46] R. Di Candia, F. Minganti, K. V. Petrovnin, G. S. Paraoanu, and S. Felicetti, Critical parametric quantum sensing, *npj Quantum Information* **9**, 23 (2023).
- [47] U. Alushi, W. Górecki, S. Felicetti, and R. Di Candia, Optimality and noise resilience of critical quantum sensing, *Phys. Rev. Lett.* **133**, 040801 (2024).

- [48] Supplemental material contains the derivation of the differential equation (3), additional numerical results for the covariance components, analytical and numerical results for the experimental detection of backaction-evading critical points and for the calculation of the continuous-monitoring Fisher information and the global Fisher information.
- [49] M.-J. Hwang, R. Puebla, and M. B. Plenio, Quantum phase transition and universal dynamics in the Rabi model, *Phys. Rev. Lett.* **115**, 180404 (2015).
- [50] L. Garbe, M. Bina, A. Keller, M. G. A. Paris, and S. Felicetti, Critical quantum metrology with a finite-component quantum phase transition, *Phys. Rev. Lett.* **124**, 120504 (2020).
- [51] S. Felicetti and A. Le Boité, Universal spectral features of ultrastrongly coupled systems, *Phys. Rev. Lett.* **124**, 040404 (2020).
- [52] N. Lambert, C. Emary, and T. Brandes, Entanglement and the phase transition in single-mode superradiance, *Phys. Rev. Lett.* **92**, 073602 (2004).
- [53] P. Ribeiro, J. Vidal, and R. Mosseri, Thermodynamical limit of the Lipkin-Meshkov-Glick model, *Phys. Rev. Lett.* **99**, 050402 (2007).
- [54] L. Cortez, A. Chantasri, L. P. García-Pintos, J. Dressel, and A. N. Jordan, Rapid estimation of drifting parameters in continuously measured quantum systems, *Phys. Rev. A* **95**, 012314 (2017).
- [55] J. Amorós-Binefa and J. Kołodyński, Noisy atomic magnetometry in real time, *New Journal of Physics* **23**, 123030 (2021).
- [56] J. Amorós-Binefa and J. Kołodyński, Noisy atomic magnetometry with Kalman filtering and measurement-based feedback, *PRX Quantum* **6**, 030331 (2025).
- [57] J. Amorós-Binefa, M. W. Mitchell, and J. Kołodyński, [Tracking time-varying signals with quantum-enhanced atomic magnetometers](#) (2025), [arXiv:2503.14793 \[quant-ph\]](#).
- [58] J. Duan, Z. Hu, X. Lu, L. Xiao, S. Jia, K. Mølmer, and Y. Xiao, Concurrent spin squeezing and field tracking with machine learning, *Nature Physics* **21**, 909 (2025).
- [59] S. Gammelmark, B. Julsgaard, and K. Mølmer, Past quantum states of a monitored system, *Phys. Rev. Lett.* **111**, 160401 (2013).
- [60] H. Bao, J. Duan, S. Jin, X. Lu, P. Li, W. Qu, M. Wang, I. Novikova, E. E. Mikhailov, K.-F. Zhao, K. Mølmer, H. Shen, and Y. Xiao, Spin squeezing of 1011 atoms by prediction and retrodiction measurements, *Nature* **581**, 159 (2020).
- [61] C. N. Madsen, L. Valdetaro, and K. Mølmer, Quantum estimation of a time-dependent perturbation, *Phys. Rev. A* **104**, 052621 (2021).

## Supplemental Material

### I. DERIVATION OF THE DIFFERENTIAL EQUATIONS (3) FOR THE MEAN VECTOR AND THE COVARIANCE MATRIX

In this section, we provide additional details for deriving the differential equations in Eq. (3) from the SME (2). It is straightforward to show that in the limit  $\chi \rightarrow 0$  the commutator  $-i[H_\omega, \rho_c]$  and the Lindblad dissipator  $\kappa\mathcal{D}[a]\rho_c$  in the SME (2) give rise to the terms  $\mathbf{A}\mathbf{r}$  and  $\mathbf{A}\boldsymbol{\Sigma} + \boldsymbol{\Sigma}\mathbf{A}^\top + \mathbf{D}$  in Eq. (3), respectively. We therefore focus only on the derivation of the last two backaction terms  $d\mathbf{w}^\top\mathbf{B}\Delta\mathbf{a}\rho_c + \rho_c\Delta\mathbf{a}^\dagger\mathbf{B}d\mathbf{w}$  in Eq. (2).

We begin by deriving the differential equation for the mean vector  $\mathbf{r}$ . Multiplying both sides of the SME (2) by the operator  $x$  and taking the trace yields,

$$\begin{aligned} \langle x d\mathbf{w}^\top\mathbf{B}\Delta\mathbf{a} \rangle_c &= d\mathbf{w}^\top\mathbf{B}\langle x\Delta\mathbf{a} \rangle_c \\ &= \frac{1}{\sqrt{2}} d\mathbf{w}^\top\mathbf{B} \begin{pmatrix} \frac{1}{2}\Sigma_x + i(\langle xp \rangle_c - \langle x \rangle_c \langle p \rangle_c) \\ \frac{i}{2}\Sigma_x + (\langle xp \rangle_c - \langle x \rangle_c \langle p \rangle_c) \end{pmatrix} \\ &= \frac{1}{\sqrt{2}} \left( \frac{1}{2}\Sigma_x + i(\langle xp \rangle_c - \langle x \rangle_c \langle p \rangle_c), \frac{i}{2}\Sigma_x + (\langle xp \rangle_c - \langle x \rangle_c \langle p \rangle_c) \right) \mathbf{B}d\mathbf{w}, \\ \langle \Delta\mathbf{a}^\dagger\mathbf{B}d\mathbf{w}x \rangle_c &= \langle \Delta\mathbf{a}^\dagger x \rangle_c \mathbf{B}d\mathbf{w} \\ &= \frac{1}{\sqrt{2}} \left( \frac{1}{2}\Sigma_x - i(\langle px \rangle_c - \langle x \rangle_c \langle p \rangle_c), -\frac{i}{2}\Sigma_x + (\langle px \rangle_c - \langle x \rangle_c \langle p \rangle_c) \right) \mathbf{B}d\mathbf{w}. \end{aligned} \quad (\text{S1})$$

Their sum is

$$\langle x d\mathbf{w}^\top\mathbf{B}\Delta\mathbf{a} \rangle_c + \langle \Delta\mathbf{a}^\dagger\mathbf{B}d\mathbf{w}x \rangle_c = \frac{1}{\sqrt{2}} (\Sigma_x - 1, \Sigma_{xp}) \mathbf{B}d\mathbf{w}, \quad (\text{S2})$$

where the row vector  $(\Sigma_x - 1, \Sigma_{xp})$  is exactly the first row of the matrix  $\boldsymbol{\Sigma} - \mathbf{I}$  appeared in Eq. (3a). Similarly, for the quadrature  $p$ ,

$$\langle p d\mathbf{w}^\top\mathbf{B}\Delta\mathbf{a} \rangle_c + \langle \Delta\mathbf{a}^\dagger\mathbf{B}d\mathbf{w}p \rangle_c = \frac{1}{\sqrt{2}} (\Sigma_{xp}, \Sigma_p - 1) \mathbf{B}d\mathbf{w}. \quad (\text{S3})$$

Combining these two results, we arrive at the last term in Eq. (3a).

Next, we derive the differential equation for the covariance  $\boldsymbol{\Sigma}$ . Applying the Itô rule  $d(fg) = gdf + fdg + df dg$  for stochastic processes  $f$  and  $g$ , we obtain  $d\Sigma_x = 2(d\langle x^2 \rangle_c - 2\langle x \rangle_c d\langle x \rangle_c - d\langle x \rangle_c d\langle x \rangle_c)$ ,  $d\Sigma_{xp} = d\langle xp + px \rangle_c - 2\langle x \rangle_c d\langle p \rangle_c - 2\langle p \rangle_c d\langle x \rangle_c - 2d\langle x \rangle_c d\langle p \rangle_c$ , and  $d\Sigma_p = 2(d\langle p^2 \rangle_c - 2\langle p \rangle_c d\langle p \rangle_c - d\langle p \rangle_c d\langle p \rangle_c)$ . The last term  $-(\boldsymbol{\Sigma} - \mathbf{I})\mathbf{B}^2(\boldsymbol{\Sigma} - \mathbf{I})dt$  in Eq. (3b) contains  $-2d\langle x \rangle_c d\langle x \rangle_c$ ,  $-2d\langle x \rangle_c d\langle p \rangle_c$ , and  $-2d\langle p \rangle_c d\langle p \rangle_c$  as its matrix elements. This can be verified by substituting Eq. (3a) into these differentials to give

$$\begin{aligned} -2d\langle x \rangle_c d\langle x \rangle_c &= -2 \left( \frac{1}{\sqrt{2}} \right)^2 (\Sigma_x - 1, \Sigma_{xp}) \mathbf{B}d\mathbf{w}d\mathbf{w}^\top\mathbf{B} \begin{pmatrix} \Sigma_x - 1 \\ \Sigma_{xp} \end{pmatrix} + \mathcal{O}(dt^{3/2}) \\ &= -(\Sigma_x - 1, \Sigma_{xp}) \mathbf{B}^2 \begin{pmatrix} \Sigma_x - 1 \\ \Sigma_{xp} \end{pmatrix} dt + \mathcal{O}(dt^{3/2}), \\ -2d\langle p \rangle_c d\langle p \rangle_c &= -2 \left( \frac{1}{\sqrt{2}} \right)^2 (\Sigma_{xp}, \Sigma_p - 1) \mathbf{B}d\mathbf{w}d\mathbf{w}^\top\mathbf{B} \begin{pmatrix} \Sigma_{xp} \\ \Sigma_p - 1 \end{pmatrix} + \mathcal{O}(dt^{3/2}) \\ &= -(\Sigma_{xp}, \Sigma_p - 1) \mathbf{B}^2 \begin{pmatrix} \Sigma_{xp} \\ \Sigma_p - 1 \end{pmatrix} dt + \mathcal{O}(dt^{3/2}), \\ -2d\langle x \rangle_c d\langle p \rangle_c &= -2 \left( \frac{1}{\sqrt{2}} \right)^2 (\Sigma_x - 1, \Sigma_{xp}) \mathbf{B}d\mathbf{w}d\mathbf{w}^\top\mathbf{B} \begin{pmatrix} \Sigma_{xp} \\ \Sigma_p - 1 \end{pmatrix} + \mathcal{O}(dt^{3/2}) \\ &= -(\Sigma_x - 1, \Sigma_{xp}) \mathbf{B}^2 \begin{pmatrix} \Sigma_{xp} \\ \Sigma_p - 1 \end{pmatrix} dt + \mathcal{O}(dt^{3/2}), \end{aligned} \quad (\text{S4})$$

where we have performed the replacement  $d\mathbf{w}d\mathbf{w}^\top \rightarrow \mathbf{I}dt$  valid for Wiener increments.



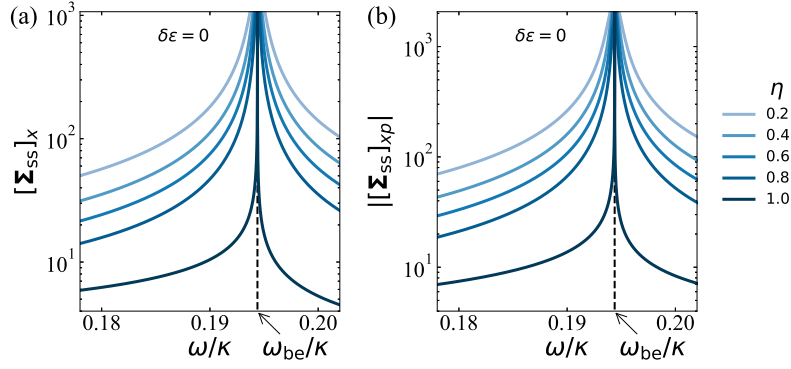


FIG. S1. The covariance components (a)  $[\Sigma_{ss}]_x$  and (b)  $|[\Sigma_{ss}]_{xp}|$  as functions of  $\omega$  for  $\varphi = 0.6$  and  $s = 0$ . The corresponding backaction-evading CP locates at  $\omega \approx 0.194\kappa$ , as marked by the dashed lines.

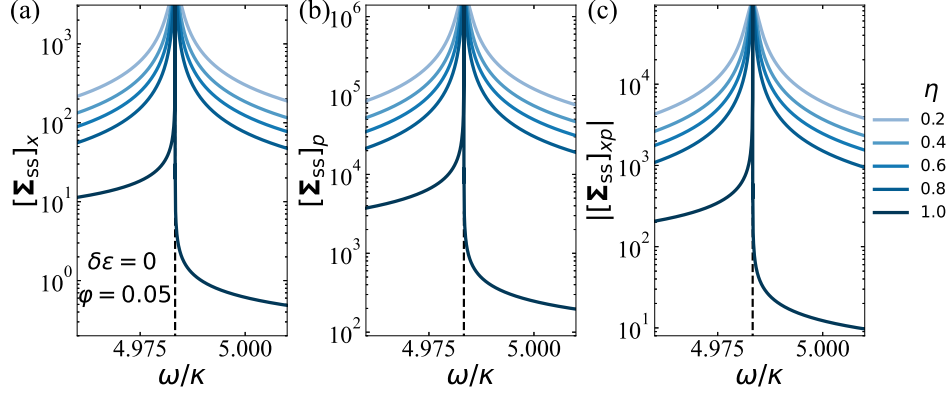


FIG. S2. The covariance components (a)  $[\Sigma_{ss}]_x$ , (b)  $[\Sigma_{ss}]_p$ , and (c)  $|[\Sigma_{ss}]_{xp}|$  as functions of  $\omega$  on the phase boundary  $\delta\epsilon = 0$  for  $\varphi = 0.05$  and  $s = 0$ . The corresponding backaction-evading CP locates at  $\omega \approx 4.983\kappa$ , as marked by the dashed lines.

## II. MORE NUMERICAL RESULTS FOR CRITICAL FLUCTUATIONS

In this section, we provide more numerical results to confirm that the existence of backaction-evading CPs is independent of the detection efficiency  $\eta$ . Fig. S1 displays the other two covariance matrix elements  $[\Sigma_{ss}]_x$  and  $|[\Sigma_{ss}]_{xp}|$  for  $\varphi = 0.6$  and  $s = 0$ , which consistently diverge at the same backaction-evading point  $\omega_{be} \approx 0.194\kappa$  as the left panel of Fig. 2(a). We further plot in Fig. S2 the three covariance components for another value of  $\varphi = 0.05$  under homodyne detection. All of these curves diverge at the backaction-evading point  $\omega_{be} \approx 4.983\kappa$  predicted by Eq. (5).

## III. EXPERIMENTAL DETECTION OF BACKACTION-EVADING CRITICAL POINTS VIA THE VARIANCE OF THE INTEGRATED CURRENT

In this section, we present analytical derivations and numerical results to demonstrate the detection of backaction-evading CPs through the variance of the integrated current,  $\mathbb{E}[\mathbf{y}_t^T \mathbf{y}_t]$ . Specifically, in Sec. III A we derive a set of deterministic differential equations to compute the variance  $\mathbb{E}[\mathbf{y}_t^T \mathbf{y}_t]$  and validate this method with numerical simulations. In Sec. III B, additional numerical results are provided, which have been used to extract the data represented by the green crosses in Fig. 1. Finally, Sec. III C offers an intuitive explanation for the origin of the minimum in  $\mathbb{E}[\mathbf{y}_t^T \mathbf{y}_t]$ .

### A. Differential equations to compute the variance of the integrated photocurrent

To derive the differential equations, we apply the Itô rule  $d(fg) = gdf + f dg + df dg$  for any stochastic processes  $f$  and  $g$ , which yields  $d\mathbb{E}[\mathbf{y}_t^T \mathbf{y}_t] = \mathbb{E}[(d\mathbf{y}_t^T) \mathbf{y}_t] + \mathbb{E}[\mathbf{y}_t^T (d\mathbf{y}_t)] + \mathbb{E}[(d\mathbf{y}_t^T)(d\mathbf{y}_t)]$ . Substituting the definition  $d\mathbf{y}_t = \sqrt{2\kappa\eta} \mathbf{B}rdt + d\mathbf{w}$

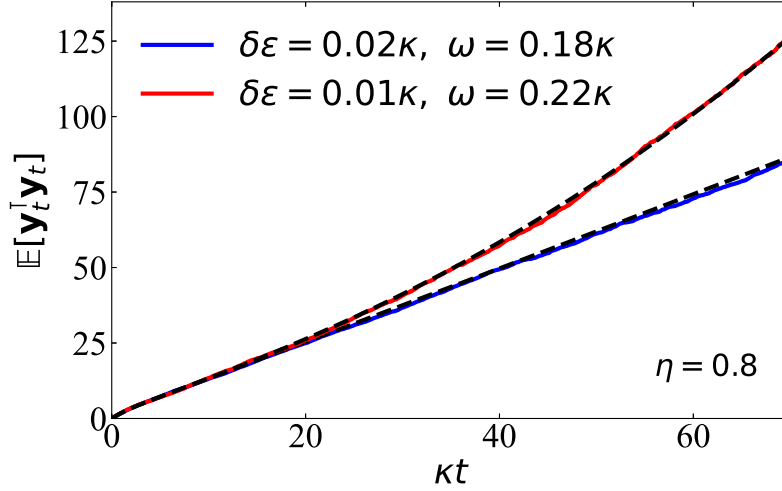


FIG. S3. Black dashed lines correspond to the results of  $\mathbb{E}[\mathbf{y}_t^T \mathbf{y}_t]$  computed by solving the deterministic differential equations Eqs. (S5-S7). Solid lines correspond to those obtained by averaging over more than 2500 photocurrent trajectories  $\mathbf{y}_t$ .

into this relation and using  $\mathbb{E}[d\mathbf{w}^T d\mathbf{w}] = 2dt$ , we obtain

$$d\mathbb{E}[\mathbf{y}_t^T \mathbf{y}_t] = \sqrt{2\kappa\eta}\mathbb{E}[\mathbf{y}_t^T \mathbf{B}\mathbf{r}]dt + \sqrt{2\kappa\eta}\mathbb{E}[\mathbf{r}^T \mathbf{B}\mathbf{y}_t]dt + 2dt = 2\sqrt{2\kappa\eta}\mathbb{E}[\mathbf{y}_t^T \mathbf{B}\mathbf{r}]dt + 2dt. \quad (\text{S5})$$

The quantity  $\mathbb{E}[\mathbf{y}_t^T \mathbf{B}\mathbf{r}]$  on the right-hand side can be expanded as a sum of  $\mathbb{E}[Xy_{1t}]$ ,  $\mathbb{E}[Xy_{2t}]$ ,  $\mathbb{E}[Py_{1t}]$  and  $\mathbb{E}[Py_{2t}]$ , where  $X = \langle x \rangle_c$  and  $P = \langle p \rangle_c$ . These four terms can be rearranged into the matrix  $\mathbb{E}[\mathbf{r}\mathbf{y}_t^T]$ . Applying the Itô rule again gives  $d\mathbb{E}[\mathbf{r}\mathbf{y}_t^T] = \mathbb{E}[(d\mathbf{r})\mathbf{y}_t^T] + \mathbb{E}[\mathbf{r}(d\mathbf{y}_t^T)] + \mathbb{E}[(d\mathbf{r})(d\mathbf{y}_t^T)]$ . Substituting Eq. (3a) and the expression for  $d\mathbf{y}_t$  into this equation leads to

$$\frac{d\mathbb{E}[\mathbf{r}\mathbf{y}_t^T]}{dt} = \mathbf{A}\mathbb{E}[\mathbf{r}\mathbf{y}_t^T] + \sqrt{2\kappa\eta}\mathbb{E}[\mathbf{r}\mathbf{r}^T]\mathbf{B} + \sqrt{\frac{\eta\kappa}{2}}(\boldsymbol{\Sigma} - \mathbf{I})\mathbf{B}. \quad (\text{S6})$$

Similarly, we derive the differential equation for the matrix  $\mathbb{E}[\mathbf{r}\mathbf{r}^T]$  appearing above

$$\frac{d\mathbb{E}[\mathbf{r}\mathbf{r}^T]}{dt} = \mathbf{A}\mathbb{E}[\mathbf{r}\mathbf{r}^T] + \mathbb{E}[\mathbf{r}\mathbf{r}^T]\mathbf{A}^T + \frac{\kappa\eta}{2}(\boldsymbol{\Sigma} - \mathbf{I})\mathbf{B}^2(\boldsymbol{\Sigma} - \mathbf{I}). \quad (\text{S7})$$

In summary, the variance of the photocurrent  $\mathbb{E}[\mathbf{y}_t^T \mathbf{y}_t]$  can be computed by solving Eqs. (S5-S7).

In Fig. S3 the results of  $\mathbb{E}[\mathbf{y}_t^T \mathbf{y}_t]$  computed by solving Eqs. (S5-S7) are plotted as black dashed lines. These are compared with the results obtained by averaging over more than 2500 photocurrent trajectories  $\mathbf{y}_t$ , which are plotted as solid lines. In both cases considered, we observe good agreement between the two methods, thereby validating the differential equations derived in Eqs. (S5-S7).

## B. More numerical results for detecting backaction-evading critical points

Here we provide additional numerical results for the variance of the integrated current  $\mathbb{E}[\mathbf{y}_t^T \mathbf{y}_t]$ . The upper panels of Fig. S4 display the time evolution of  $\mathbb{E}[\mathbf{y}_t^T \mathbf{y}_t]$  for (a)  $\delta\epsilon = 0.02\kappa$ , (b)  $\delta\epsilon = 0.01\kappa$ , and (c)  $\delta\epsilon = 0.005\kappa$  under homodyne detection with  $\varphi = 0.6$  and  $\eta = 0.8$ . The lower panels show the values of  $\mathbb{E}[\mathbf{y}_t^T \mathbf{y}_t]$  at  $\kappa t = 100$  as functions of  $\omega$ . The locations of the minima extracted from these curves are plotted as green crosses in Fig. 1.

## C. Understanding the minimum in the variance of the integrated photocurrent

In this subsection, we present a qualitative explanation for the origin of the characteristic minimum developed in the variance of the integrated photocurrent near a backaction-evading CP. Under homodyne detection ( $s = 0$ ), the matrix  $\mathbf{B}$  in Eq. (2) takes the explicit form  $\mathbf{B} = (\cos^2 \varphi, \cos \varphi \sin \varphi; \cos \varphi \sin \varphi, \sin^2 \varphi)$ . As a result, the photocurrent

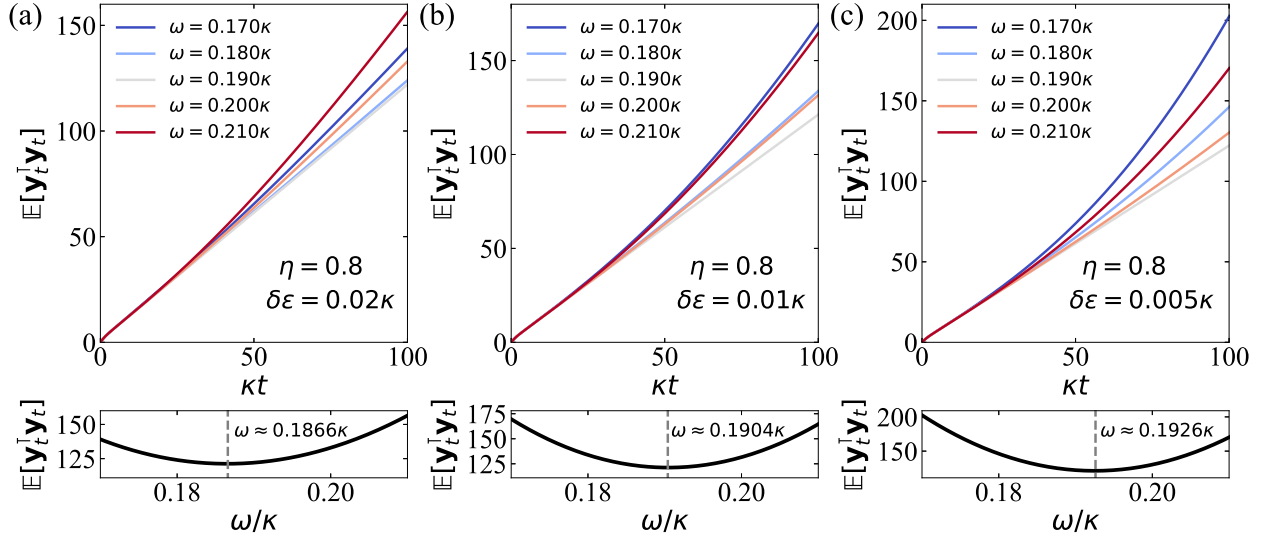


FIG. S4. Upper panels: Time evolution of the variance of the integrated current  $\mathbb{E}[\mathbf{y}_t^T \mathbf{y}_t]$  for (a)  $\delta\epsilon = 0.02\kappa$ , (b)  $\delta\epsilon = 0.01\kappa$ , and (c)  $\delta\epsilon = 0.005\kappa$ . Lower panels:  $\mathbb{E}[\mathbf{y}_t^T \mathbf{y}_t]$  at time  $\kappa t = 100$  as functions of  $\omega$ . Dashed lines correspond to the minimum locations with their values given explicitly. These minimum locations have been shown as the green crosses in Fig. 1. Here all simulations are performed under homodyne detection, i.e.,  $s = 0$ , with  $\varphi = 0.6$  and non-ideal detection efficiency  $\eta = 0.8$ .

$d\mathbf{y}_t$  under homodyne detection can be rewritten in a vector form as

$$d\mathbf{y}_t = \sqrt{2\kappa\eta} \begin{pmatrix} \cos^2 \varphi X + \cos \varphi \sin \varphi P \\ \cos \varphi \sin \varphi X + \sin^2 \varphi P \end{pmatrix} dt + d\mathbf{w} = \sqrt{2\kappa\eta} \begin{pmatrix} \cos \varphi X_\varphi \\ \sin \varphi X_\varphi \end{pmatrix} dt + d\mathbf{w}, \quad (\text{S8})$$

where  $X = \langle x \rangle_c$ ,  $P = \langle p \rangle_c$ , and  $X_\varphi = \langle x_\varphi \rangle_c = \cos \varphi X + \sin \varphi P$  with  $x_\varphi = \cos \varphi x + \sin \varphi p$ . We can apply the rotation  $\mathbf{R}_\varphi$  to define a new photocurrent  $d\mathbf{y}'_t = \mathbf{R}_\varphi d\mathbf{y}_t$ , which takes the explicit form

$$d\mathbf{y}'_t = \sqrt{2\kappa\eta} \begin{pmatrix} X_\varphi dt \\ 0 \end{pmatrix} + \mathbf{R}_\varphi d\mathbf{w} = \sqrt{2\kappa\eta} \begin{pmatrix} X_\varphi dt + dw'_1 \\ dw'_2 \end{pmatrix}, \quad (\text{S9})$$

where we have introduced two new independent Wiener increments  $dw'_1 = \cos \varphi dw_1 + \sin \varphi dw_2$  and  $dw'_2 = -\sin \varphi dw_1 + \cos \varphi dw_2$ . This expression shows that one output port carries the standard homodyne current,  $dy_{\text{hom}} \equiv [d\mathbf{y}'_t]_1 = \sqrt{2\kappa\eta} X_\varphi + dw'_1$ , while the other exports only white noise, containing no information of the observable  $x_\varphi$ .

From this perspective, the variance  $\mathbb{E}[\mathbf{y}_t^T \mathbf{y}_t]$  is related to the variances of  $X_\varphi$  and its conjugate quadrature  $P_\varphi = -\sin \varphi X + \cos \varphi P$ . The dependence on  $P_\varphi$  arises because, in the integrated homodyne current  $y_{\text{hom}} = \sqrt{2\kappa\eta} \int_0^t X_\varphi d\tau + w'_1(t)$ , the term  $\int_0^t X_\varphi d\tau$  is implicitly correlated with  $w'_1(t)$ , in other words, they are not independent random variables, as seen in Eq. (3). As a consequence, the behavior of  $\mathbb{E}[\mathbf{y}_t^T \mathbf{y}_t]$  can be qualitatively understood from the variances of  $X_\varphi$  and  $P_\varphi$ .

We recall that the initial state is chosen as the vacuum, so the quantum expectation value of an arbitrary quadrature operator  $x_\phi$ , denoted as  $X_\phi = \text{Tr}[x_\phi \rho_c]$ , is a random variable with zero mean in the long-time limit, i.e.,  $\lim_{t \rightarrow \infty} \mathbb{E}[X_\phi] = \lim_{t \rightarrow \infty} \mathbb{E}[\text{Tr}(x_\phi \rho_c)] = \lim_{t \rightarrow \infty} \text{Tr}(x_\phi \rho_0) = 0$ , where  $\rho_0 = \mathbb{E}[\rho_c]$  is the unconditional state. The variance of  $X_\phi$  is therefore simply  $\mathbb{E}[X_\phi^2]$ , which can be further decomposed as

$$\mathbb{E}[X_\phi^2] = \text{Tr}[x_\phi^2 \rho_0] - \mathbb{E}[\Sigma_{x_\phi}] = \text{Tr}[x_\phi^2 \rho_0] - \Sigma_{x_\phi}, \quad (\text{S10})$$

where we have used the property  $\mathbb{E}[\Sigma_{x_\phi}] = \Sigma_{x_\phi}$  in the Gaussian limit  $\chi \rightarrow 0$ . Eq. (S10) hints distinct behaviors of  $\mathbb{E}[\mathbf{y}_t^T \mathbf{y}_t]$  near and away from a backaction-evading CP. Near such a CP, the difference  $\text{Tr}[x_\phi^2 \rho_0] - \Sigma_{x_\phi}$  is small, as shown in the right panel of Fig. 2, leading to less fluctuated  $X_\phi$ . In contrast, away from a backaction-evading CP,  $X_\phi$  exhibits a larger variance. Accordingly, the integrated photocurrent  $\mathbf{y}_t$  is expected to behave differently in these two regimes. Although the reasoning presented here does not fully account for the minima in  $\mathbb{E}[\mathbf{y}_t^T \mathbf{y}_t]$ , it supports our idea of detecting backaction-evading CPs through such minima when combined with the numerical results provided earlier.

#### IV. CALCULATION OF THE FISHER INFORMATION AND THE GLOBAL FISHER INFORMATION

In this section, we provide details for calculating the continuous-monitoring FI  $F(\varphi, s)$  and the global QFI  $I_G$ . In Sec. IV A, we derive a set of coupled, deterministic differential equations for calculating  $F(\varphi, s)$ . In Sec. IV B, we provide an alternative approach to calculate the global QFI  $I_G$  which is valid in the limit  $\chi \rightarrow 0$ . Using this approach, we are able to prove rigorously that  $I_G$  is asymptotically linear in time,  $I_G \sim k_G t$ . We also derive an analytical expression for the slope  $k_G$ .

##### A. The continuous-monitoring Fisher information

As mentioned in the main text, for positive frequencies  $\omega > 0$ , the scaling limit  $\chi \rightarrow 0$  in the normal phase ( $\epsilon < \epsilon_c$  or equivalently  $\delta\epsilon > 0$ ) is reached by simply setting  $\chi = 0$  in the Kerr Hamiltonian (1). In this case, the open KPO we considered is a linear Gaussian system. In addition, since continuous general-dyne monitoring falls within the class of Gaussian measurements, the resulting photocurrent record  $\mathbf{y}_{\leq t}$  follows a Gaussian probability distribution  $p_{\text{gd}}(\mathbf{y}_{\leq t}|\omega)$ . In a recent study [44], Genoni showed that under such conditions the FI  $F(\varphi, s)$  associated with the Gaussian likelihood  $p_{\text{gd}}(\mathbf{y}_{\leq t}|\omega)$  can be computed using the formula in Eq. (6).

Although Eq. (6) is formally concise, it requires taking an ensemble average, which can still be numerically expensive. However, if the integrand  $\mathbb{E}[(\partial_\omega \mathbf{r}^\top) \mathbf{B}^2 (\partial_\omega \mathbf{r})]$  can be solved, the FI  $F(\varphi, s)$  can be obtained by numerically integrating this quantity. Below, we show that this is possible due to the Gaussian nature of the monitored open KPO under continuous general-dyne detection. Specifically, we derive a set of coupled, deterministic differential equations for the quantities  $\mathbb{E}[\mathbf{r} \mathbf{r}^\top]$ ,  $\mathbb{E}[(\partial_\omega \mathbf{r})(\partial_\omega \mathbf{r}^\top)]$  and  $\mathbb{E}[(\partial_\omega \mathbf{r}) \mathbf{r}^\top]$ . Then the integrand  $\mathbb{E}[(\partial_\omega \mathbf{r}^\top) \mathbf{B}^2 (\partial_\omega \mathbf{r})]$  can be constructed from the numerical solution of  $\mathbb{E}[(\partial_\omega \mathbf{r})(\partial_\omega \mathbf{r}^\top)]$  together with the expression of the matrix  $\mathbf{B}$ .

To derive the aforementioned equations, we first differentiate both sides of Eq. (3) with respect to the frequency  $\omega$ , yielding

$$d(\partial_\omega \mathbf{r}) = (\partial_\omega \mathbf{A}) \mathbf{r} dt + \mathbf{A} (\partial_\omega \mathbf{r}) dt + \sqrt{\frac{\kappa \eta}{2}} (\partial_\omega \boldsymbol{\Sigma}) \mathbf{B} d\mathbf{w} - \kappa \eta (\boldsymbol{\Sigma} - \mathbf{I}) \mathbf{B}^2 (\partial_\omega \mathbf{r}) dt, \quad (\text{S11a})$$

$$\frac{d(\partial_\omega \boldsymbol{\Sigma})}{dt} = (\mathbf{A} + \kappa \eta \mathbf{B}^2) (\partial_\omega \boldsymbol{\Sigma}) + (\partial_\omega \boldsymbol{\Sigma}) (\mathbf{A}^\top + \kappa \eta \mathbf{B}^2) - \kappa \eta (\partial_\omega \boldsymbol{\Sigma}) \mathbf{B}^2 \boldsymbol{\Sigma} - \kappa \eta \boldsymbol{\Sigma} \mathbf{B}^2 (\partial_\omega \boldsymbol{\Sigma}) + (\partial_\omega \mathbf{A}) \boldsymbol{\Sigma} + \boldsymbol{\Sigma} (\partial_\omega \mathbf{A}^\top). \quad (\text{S11b})$$

We note that in deriving Eq. (S11a), the Wiener increment  $d\mathbf{w}$  in Eq. (3a) has been replaced by the current formula  $d\mathbf{w} = d\mathbf{y}_t - \sqrt{2\eta\kappa} \mathbf{B} \mathbf{r} dt$ , and the property  $\partial_\omega (d\mathbf{y}_t) = 0$  has been used. Applying the Itô rule  $d(fg) = gdf + fdg + dfdg$  for stochastic processes  $f$  and  $g$ , we obtain the following differential relations:  $d\mathbb{E}[\mathbf{r} \mathbf{r}^\top] = \mathbb{E}[(d\mathbf{r}) \mathbf{r}^\top] + \mathbb{E}[\mathbf{r} (d\mathbf{r}^\top)] + \mathbb{E}[(d\mathbf{r})(d\mathbf{r}^\top)]$ ,  $d\mathbb{E}[(\partial_\omega \mathbf{r})(\partial_\omega \mathbf{r}^\top)] = \mathbb{E}[(d\partial_\omega \mathbf{r})(\partial_\omega \mathbf{r}^\top)] + \mathbb{E}[(\partial_\omega \mathbf{r})(d\partial_\omega \mathbf{r}^\top)] + \mathbb{E}[(d\partial_\omega \mathbf{r})(d\partial_\omega \mathbf{r}^\top)]$ , and  $d\mathbb{E}[(\partial_\omega \mathbf{r}) \mathbf{r}^\top] = \mathbb{E}[(d\partial_\omega \mathbf{r}) \mathbf{r}^\top] + \mathbb{E}[(\partial_\omega \mathbf{r}) d\mathbf{r}^\top] + \mathbb{E}[(d\partial_\omega \mathbf{r}) d\mathbf{r}^\top]$ . Finally, substituting Eqs. (3) and (S11) into these relations leads to the promised set of deterministic differential equations

$$\begin{aligned} \frac{d\mathbb{E}[\mathbf{r} \mathbf{r}^\top]}{dt} &= \mathbf{A} \mathbb{E}[\mathbf{r} \mathbf{r}^\top] + \mathbb{E}[\mathbf{r} \mathbf{r}^\top] \mathbf{A}^\top + \frac{\kappa \eta}{2} (\boldsymbol{\Sigma} - \mathbf{I}) \mathbf{B}^2 (\boldsymbol{\Sigma} - \mathbf{I}), \\ \frac{d\mathbb{E}[(\partial_\omega \mathbf{r})(\partial_\omega \mathbf{r}^\top)]}{dt} &= (\partial_\omega \mathbf{A}) \mathbb{E}[\mathbf{r} (\partial_\omega \mathbf{r}^\top)] + \mathbf{A} \mathbb{E}[(\partial_\omega \mathbf{r})(\partial_\omega \mathbf{r}^\top)] - \kappa \eta (\boldsymbol{\Sigma} - \mathbf{I}) \tilde{\mathbf{B}}^2 \mathbb{E}[(\partial_\omega \mathbf{r})(\partial_\omega \mathbf{r}^\top)] \\ &\quad + \mathbb{E}[(\partial_\omega \mathbf{r}) \mathbf{r}^\top] (\partial_\omega \mathbf{A}^\top) + \mathbb{E}[(\partial_\omega \mathbf{r})(\partial_\omega \mathbf{r}^\top)] \mathbf{A}^\top - \kappa \eta \mathbb{E}[(\partial_\omega \mathbf{r})(\partial_\omega \mathbf{r}^\top)] \mathbf{B}^2 (\boldsymbol{\Sigma} - \mathbf{I}) + \frac{\kappa \eta}{2} (\partial_\omega \boldsymbol{\Sigma}) \mathbf{B}^2 (\partial_\omega \boldsymbol{\Sigma}), \\ \frac{d\mathbb{E}[(\partial_\omega \mathbf{r}) \mathbf{r}^\top]}{dt} &= (\partial_\omega \mathbf{A}) \mathbb{E}[\mathbf{r} \mathbf{r}^\top] + \mathbf{A} \mathbb{E}[(\partial_\omega \mathbf{r}) \mathbf{r}^\top] - \kappa \eta (\boldsymbol{\Sigma} - \mathbf{I}) \mathbf{B}^2 \mathbb{E}[(\partial_\omega \mathbf{r}) \mathbf{r}^\top] + \mathbb{E}[(\partial_\omega \mathbf{r}) \mathbf{r}^\top] \mathbf{A}^\top + \frac{\kappa \eta}{2} (\partial_\omega \boldsymbol{\Sigma}) \mathbf{B}^2 (\boldsymbol{\Sigma} - \mathbf{I}). \end{aligned} \quad (\text{S12})$$

These equations can then be integrated to obtain the solution of the integrand in Eq. (6).

##### B. The global quantum Fisher information

While Eq. (8) provides a numerically tractable method for computing the global QFI  $I_G$ , we find in practical simulations that solving  $\mu_{\omega_1, \omega_2}$  can still be challenging under certain conditions, especially near the phase boundary and/or at long evolution times. Here, we present an alternative approach valid in the scaling limit  $\chi \rightarrow 0$ . This approach allows us to rigorously prove that  $I_G$  grows linearly at long times,  $I_G \sim k_G t$ , and to derive a compact expression for the corresponding growth rate  $k_G$ .



We begin by re-expressing the functional dependence of  $\mu_{\omega_1, \omega_2}$  on  $\omega_1$  and  $\omega_2$  in terms of their average  $\bar{\omega} = (\omega_1 + \omega_2)/2$  and half-difference  $\delta\omega = (\omega_2 - \omega_1)/2$ , i.e.,  $\mu_{\omega_1, \omega_2} = \mu_{\bar{\omega}, \delta\omega}$ . Accordingly, Eq. (8) becomes

$$\frac{d\mu_{\bar{\omega}, \delta\omega}}{dt} = -i[H_{\bar{\omega}}, \mu_{\bar{\omega}, \delta\omega}] + i\{\delta\omega a^\dagger a, \mu_{\bar{\omega}, \delta\omega}\} + \kappa\mathcal{D}[a]\mu_{\bar{\omega}, \delta\omega}. \quad (\text{S13})$$

This change of variable also allows us to rewrite the derivatives in the definition of  $I_G$  as

$$I_G = 4\partial_{\omega_1}\partial_{\omega_2}\ln|\text{Tr}[\mu_{\omega_1, \omega_2}]|_{\omega_1=\omega_2=\omega} = (\partial_{\bar{\omega}}^2 - \partial_{\delta\omega}^2)\ln|\text{Tr}[\mu_{\bar{\omega}, \delta\omega}]|_{\bar{\omega}=\omega, \delta\omega=0}. \quad (\text{S14})$$

Since  $\mu_{\bar{\omega}, \delta\omega}|_{\delta\omega=0}$  coincides with the unconditional reduced density matrix  $\rho_0$  of the open KPO, i.e.,  $\mu_{\bar{\omega}, \delta\omega}|_{\delta\omega=0} = \rho_0$ , it preserve unity trace,  $\text{Tr}[\mu_{\bar{\omega}, \delta\omega}]|_{\delta\omega=0} = 1$ . This leads to the simplified expression

$$I_G = -\partial_{\delta\omega}^2\ln|\text{Tr}[\mu_{\omega, \delta\omega}]|_{\delta\omega=0}. \quad (\text{S15})$$

Using the identity  $|\text{Tr}[\mu_{\omega, \delta\omega}]| = \sqrt{\text{Tr}[\mu_{\omega, \delta\omega}]\text{Tr}[\mu_{\omega, \delta\omega}^\dagger]}$ , we obtain

$$\begin{aligned} I_G &= -\frac{1}{2}\partial_{\delta\omega}^2\left(\ln\text{Tr}[\mu_{\omega, \delta\omega}] + \log\text{Tr}[\mu_{\omega, \delta\omega}^\dagger]\right)\Big|_{\delta\omega=0} \\ &= -\frac{1}{2}\left[\text{Tr}[\partial_{\delta\omega}^2\mu_{\omega, \delta\omega}]|_{\delta\omega=0} + \text{Tr}[\partial_{\delta\omega}^2\mu_{\omega, \delta\omega}^\dagger]|_{\delta\omega=0} - (\text{Tr}[\partial_{\delta\omega}\mu_{\omega, \delta\omega}]|_{\delta\omega=0})^2 - (\text{Tr}[\partial_{\delta\omega}\mu_{\omega, \delta\omega}^\dagger]|_{\delta\omega=0})^2\right] \\ &= -\text{Re}\left[\text{Tr}[\partial_{\delta\omega}^2\mu_{\omega, \delta\omega}]|_{\delta\omega=0} - (\text{Tr}[\partial_{\delta\omega}\mu_{\omega, \delta\omega}]|_{\delta\omega=0})^2\right]. \end{aligned} \quad (\text{S16})$$

Consequently,  $I_G$  can be computed by solving for the two generalized matrices  $\partial_{\delta\omega}^2\mu_{\omega, \delta\omega}|_{\delta\omega=0}$  and  $\partial_{\delta\omega}\mu_{\omega, \delta\omega}|_{\delta\omega=0}$ . In the following, we define  $\mu = \mu_{\omega, \delta\omega}|_{\delta\omega=0}$ ,  $\partial_{\delta\omega}^2\mu = \partial_{\delta\omega}^2\mu_{\omega, \delta\omega}|_{\delta\omega=0}$ , and  $\partial_{\delta\omega}\mu = \partial_{\delta\omega}\mu_{\omega, \delta\omega}|_{\delta\omega=0}$  to simplify the notations.

The differential equations for  $\partial_{\delta\omega}^2\mu$  and  $\partial_{\delta\omega}\mu$  can be readily obtained by taking respectively the first and second derivative with respect to  $\delta\omega$  on both sides of Eq. (S13), and then setting  $\bar{\omega} = \omega$ ,  $\delta\omega = 0$ . This procedure yields

$$\frac{d\mu}{dt} = -i[H_\omega, \mu] + \kappa\mathcal{D}[a]\mu, \quad (\text{S17a})$$

$$\frac{d(\partial_{\delta\omega}\mu)}{dt} = -i[H_\omega, \partial_{\delta\omega}\mu] + i\{a^\dagger a, \mu\} + \kappa\mathcal{D}[a]\partial_{\delta\omega}\mu, \quad (\text{S17b})$$

$$\frac{d(\partial_{\delta\omega}^2\mu)}{dt} = -i[H_\omega, \partial_{\delta\omega}^2\mu] + 2i\{a^\dagger a, \partial_{\delta\omega}\mu\} + \kappa\mathcal{D}[a]\partial_{\delta\omega}^2\mu, \quad (\text{S17c})$$

where we have also written explicitly the equation satisfied by  $\mu$  for later convenience. We reiterate that  $\mu$  coincides with the unconditional reduced density matrix  $\rho_0$ . Since only  $\text{Tr}[\partial_{\delta\omega}^2\mu]$  is needed in Eq. (S16), we take trace on both sides of Eq. (S17c) to get

$$\frac{d\text{Tr}[\partial_{\delta\omega}^2\mu]}{dt} = 2i\text{Tr}[\{a^\dagger a, \partial_{\delta\omega}\mu\}] = 4i\text{Tr}[a^\dagger a\partial_{\delta\omega}\mu], \quad (\text{S18})$$

which relates  $\text{Tr}[\partial_{\delta\omega}^2\mu]$  to the moment  $\text{Tr}[a^\dagger a\partial_{\delta\omega}\mu]$  of  $\partial_{\delta\omega}\mu$ .

The above analysis shows that the calculation of the global QFI  $I_G$  requires only the knowledge of  $\text{Tr}[\partial_{\delta\omega}\mu]$  and  $\text{Tr}[a^\dagger a\partial_{\delta\omega}\mu]$ . For the Kerr Hamiltonian (1), the solution  $\partial_{\delta\omega}\mu$  of Eq. (S17b) in the limit  $\chi \rightarrow 0$  remains Gaussian since  $\partial_{\delta\omega}\mu = 0$  at the initial time. As a result, the moments  $\langle a^\dagger a \rangle_{\partial_{\delta\omega}\mu}$ ,  $\langle a^{\dagger 2} - a^2 \rangle_{\partial_{\delta\omega}\mu}$ ,  $\langle a^{\dagger 2} + a^2 \rangle_{\partial_{\delta\omega}\mu}$  and  $\langle 1 \rangle_{\partial_{\delta\omega}\mu}$  obey the following closed-form differential equations

$$\begin{aligned} \frac{d\langle a^\dagger a \rangle_{\partial_{\delta\omega}\mu}}{dt} &= -i\epsilon\langle a^{\dagger 2} - a^2 \rangle_{\partial_{\delta\omega}\mu} - \kappa\langle a^\dagger a \rangle_{\partial_{\delta\omega}\mu} + 2i\langle (a^\dagger a)^2 \rangle_{\mu}, \\ \frac{d\langle a^{\dagger 2} + a^2 \rangle_{\partial_{\delta\omega}\mu}}{dt} &= 2i\omega\langle a^{\dagger 2} - a^2 \rangle_{\partial_{\delta\omega}\mu} - \kappa\langle a^{\dagger 2} + a^2 \rangle_{\partial_{\delta\omega}\mu} + 2i\langle a^{\dagger 3} a + a^\dagger a^3 + a^{\dagger 2} + a^2 \rangle_{\mu}, \\ \frac{d\langle a^{\dagger 2} - a^2 \rangle_{\partial_{\delta\omega}\mu}}{dt} &= 2i\omega\langle a^{\dagger 2} + a^2 \rangle_{\partial_{\delta\omega}\mu} + 4i\epsilon\langle a^\dagger a \rangle_{\partial_{\delta\omega}\mu} + 2i\epsilon\langle 1 \rangle_{\partial_{\delta\omega}\mu} - \kappa\langle a^{\dagger 2} - a^2 \rangle_{\partial_{\delta\omega}\mu} + 2i\langle a^{\dagger 3} a - a^\dagger a^3 + a^{\dagger 2} - a^2 \rangle_{\mu}, \\ \frac{d\langle 1 \rangle_{\partial_{\delta\omega}\mu}}{dt} &= 2i\langle a^\dagger a \rangle_{\mu}, \end{aligned} \quad (\text{S19})$$

where  $\langle O \rangle_{\partial_{\delta\omega}\mu} = \text{Tr}[O\partial_{\delta\omega}\mu]$  and  $\langle O \rangle_{\mu} = \text{Tr}[O\mu]$  are expectations of an operator  $O$  with respect to  $\partial_{\delta\omega}\mu$  and  $\mu$ , respectively, and  $\langle 1 \rangle_{\partial_{\delta\omega}\mu} = \text{Tr}[\partial_{\delta\omega}\mu]$  denotes the trace of the matrix  $\partial_{\delta\omega}\mu$ .

The moments  $\langle (a^\dagger a)^2 \rangle_{\mu}$ ,  $\langle a^{\dagger 3} a + a^\dagger a^3 + a^{\dagger 2} + a^2 \rangle_{\mu}$ ,  $\langle a^{\dagger 3} a - a^\dagger a^3 + a^{\dagger 2} - a^2 \rangle_{\mu}$ , and  $\langle a^\dagger a \rangle_{\mu}$  with respect to  $\mu$  appeared in Eq. (S19) can be readily evaluated using the method of Langevin equations. To keep the presentation concise, we postpone their derivation to a later subsection in Sec. IV C. The last equation in Eq. (S19) can be directly integrated to yield the solution of  $\langle 1 \rangle_{\partial_{\delta\omega}\mu}$ , written explicitly as

$$\begin{aligned} \langle 1 \rangle_{\partial_{\delta\omega}\mu} &= 2i \int_0^t d\tau \langle a^\dagger a \rangle_{\mu} \\ &= 2i|\gamma_c|^2 \left( \frac{1 - e^{-2\text{Re}\lambda_- t}}{2\text{Re}\lambda_-} + \frac{1 - e^{-2\text{Re}\lambda_+ t}}{2\text{Re}\lambda_+} - 2\text{Re} \frac{1 - e^{-(\lambda_- + \lambda_+^*)t}}{\lambda_- + \lambda_+^*} \right) + 2i\kappa|\gamma_c|^2 \left( \frac{2\text{Re}\lambda_- t - 1 + e^{-2\text{Re}\lambda_- t}}{4\text{Re}^2\lambda_-} \right. \\ &\quad \left. + \frac{2\text{Re}\lambda_+ t - 1 + e^{-2\text{Re}\lambda_+ t}}{4\text{Re}^2\lambda_+} - \frac{(\lambda_- + \lambda_+^*)t - 1 + e^{-(\lambda_- + \lambda_+^*)t}}{(\lambda_- + \lambda_+^*)^2} - \frac{(\lambda_-^* + \lambda_+)t - 1 + e^{-(\lambda_-^* + \lambda_+)t}}{(\lambda_-^* + \lambda_+)^2} \right). \end{aligned} \quad (\text{S20})$$

Definitions of the variables  $\lambda_{\pm}$  and  $\gamma_c$  are given in Sec. IV C.

Defining the vector  $\mathbf{v} = (\langle a^\dagger a \rangle_{\partial_{\delta\omega}\mu}, \langle a^{\dagger 2} + a^2 \rangle_{\partial_{\delta\omega}\mu}, \langle a^{\dagger 2} - a^2 \rangle_{\partial_{\delta\omega}\mu})^\top$ , we can recast the first three equations in Eq. (S19) into the vector form

$$\frac{d\mathbf{v}}{dt} = \mathbf{M}\mathbf{v} + 2i\mathbf{f}(t), \quad (\text{S21})$$

where we have introduced the  $3 \times 3$  matrix  $\mathbf{M}$  and the time-dependent vector  $\mathbf{f}(t)$ ,

$$\mathbf{M} = \begin{pmatrix} -\kappa & 0 & -i\epsilon \\ 0 & -\kappa & 2i\omega \\ 4i\epsilon & 2i\omega & -\kappa \end{pmatrix}, \quad \mathbf{f}(t) = \begin{pmatrix} f_1 \\ f_2 \\ f_3 \end{pmatrix} = \begin{pmatrix} \langle (a^\dagger a)^2 \rangle_{\mu} \\ \langle a^{\dagger 3} a + a^\dagger a^3 + a^{\dagger 2} + a^2 \rangle_{\mu} \\ \langle a^{\dagger 3} a - a^\dagger a^3 + a^{\dagger 2} - a^2 \rangle_{\mu} + \epsilon \langle 1 \rangle_{\partial_{\delta\omega}\mu} \end{pmatrix}. \quad (\text{S22})$$

Explicit expressions of the components  $f_i$  ( $i = 1, 2, 3$ ) are given in Sec. IV C. This vector equation can be readily solved to yield

$$\mathbf{v}(t) = e^{\mathbf{M}t}\mathbf{v}(0) + 2ie^{\mathbf{M}t} \int_0^t d\tau e^{-\mathbf{M}\tau}\mathbf{f}(\tau). \quad (\text{S23})$$

The solution of  $\langle a^\dagger a \rangle_{\partial_{\delta\omega}\mu}$  is simply the first component of  $\mathbf{v}(t)$ , which has the explicit expression

$$\begin{aligned} \langle a^\dagger a \rangle_{\partial_{\delta\omega}\mu}(t) &= 2i \int_0^t d\tau \left[ -e^{-\kappa(t-\tau)} \frac{\omega^2 f_1(\tau) + \omega\epsilon f_2(\tau)/2}{\epsilon^2 - \omega^2} + e^{-(\kappa+2\sqrt{\epsilon^2-\omega^2})(t-\tau)} \frac{2\epsilon^2 f_1(\tau) + \omega\epsilon f_2(\tau) + i\epsilon\sqrt{\epsilon^2-\omega^2} f_3(\tau)}{4(\epsilon^2 - \omega^2)} \right. \\ &\quad \left. + e^{-(\kappa-2\sqrt{\epsilon^2-\omega^2})(t-\tau)} \frac{2\epsilon^2 f_1(\tau) + \omega\epsilon f_2(\tau) - i\epsilon\sqrt{\epsilon^2-\omega^2} f_3(\tau)}{4(\epsilon^2 - \omega^2)} \right]. \end{aligned} \quad (\text{S24})$$

Substituting it back into Eq. (S18), we ultimately obtain

$$\begin{aligned} \text{Tr}[\partial_{\delta\omega}^2\mu] &= 4i \int_0^t ds \langle a^\dagger a \rangle_{\partial_{\delta\omega}\mu} \\ &= -8 \int_0^t ds \int_0^s d\tau \left[ -e^{-\kappa(s-\tau)} \frac{\omega^2 f_1(\tau) + \omega\epsilon f_2(\tau)/2}{\epsilon^2 - \omega^2} + e^{-(\kappa+2\sqrt{\epsilon^2-\omega^2})(s-\tau)} \frac{2\epsilon^2 f_1(\tau) + \omega\epsilon f_2(\tau) + i\epsilon\sqrt{\epsilon^2-\omega^2} f_3(\tau)}{4(\epsilon^2 - \omega^2)} \right. \\ &\quad \left. + e^{-(\kappa-2\sqrt{\epsilon^2-\omega^2})(s-\tau)} \frac{2\epsilon^2 f_1(\tau) + \omega\epsilon f_2(\tau) - i\epsilon\sqrt{\epsilon^2-\omega^2} f_3(\tau)}{4(\epsilon^2 - \omega^2)} \right]. \end{aligned} \quad (\text{S25})$$

Eqs. (S20) and (S25) provides the solutions of  $\langle 1 \rangle_{\partial_{\delta\omega}\mu}$  and  $\text{Tr}[\partial_{\delta\omega}^2\mu]$ , which can then be substituted in Eq. (S16) to obtain the global QFI  $I_G$ .

### 1. Long-time behavior

With the solutions in Eqs. (S20) and (S25) available, we now analyze the long-time behavior of the global QFI  $I_G$ .

We first prove that at long times  $I_G$  scales linearly,  $I_G \sim k_G t$ . To this end, we extract from Eq. (S20) and (S25) the leading long-time contribution of  $\langle 1 \rangle_{\partial_{\delta\omega\mu}}$  and  $\langle 1 \rangle_{\partial_{\delta\omega}^2}$ ,

$$\langle 1 \rangle_{\partial_{\delta\omega\mu}} \sim 2i\kappa|\gamma_c|^2 \left( \frac{\text{Re}(\lambda_+ + \lambda_-)}{2\text{Re}\lambda_- \text{Re}\lambda_+} - \frac{2\text{Re}(\lambda_- + \lambda_+^*)}{|\lambda_- + \lambda_+^*|^2} \right) t, \quad (\text{S26})$$

$$\langle 1 \rangle_{\partial_{\delta\omega}^2} \sim -\frac{8\epsilon^2\kappa|\gamma_c|^2}{\kappa^2 - 4(\epsilon^2 - \omega^2)} \left( \frac{\text{Re}(\lambda_+ + \lambda_-)}{2\text{Re}\lambda_- \text{Re}\lambda_+} - \frac{2\text{Re}(\lambda_- + \lambda_+^*)}{|\lambda_- + \lambda_+^*|^2} \right) t^2. \quad (\text{S27})$$

Substituting these asymptotic forms into Eq. (S16) and using the definitions of  $\lambda_{\pm}$  and  $\gamma_c$  from Sec. IV C, it follows directly that  $I_G$  grows at most quadratically in time. Furthermore, a direct calculation of the quadratic contribution of  $I_G$  yields

$$\frac{8\epsilon^2\kappa|\gamma_c|^2}{\kappa^2 - 4(\epsilon^2 - \omega^2)} \left( \frac{\text{Re}(\lambda_+ + \lambda_-)}{2\text{Re}\lambda_- \text{Re}\lambda_+} - \frac{2\text{Re}(\lambda_- + \lambda_+^*)}{|\lambda_- + \lambda_+^*|^2} \right) t^2 - 4\kappa^2|\gamma_c|^4 \left( \frac{\text{Re}(\lambda_+ + \lambda_-)}{2\text{Re}\lambda_- \text{Re}\lambda_+} - \frac{2\text{Re}(\lambda_- + \lambda_+^*)}{|\lambda_- + \lambda_+^*|^2} \right)^2 t^2 = 0, \quad (\text{S28})$$

which shows that the quadratic term vanishes. We therefore conclude that  $I_G$  grows linearly in the long-time limit.

Next, we derive an analytical expression for the growth rate  $k_G$ . The calculation is straightforward but lengthy, so we omit the intermediate steps and summarize only the final result. Numerical validation will be provided in the following subsection. Specifically, the growth rate is given by

$$k_G = \text{Re}(-k_{G,1} - k_{G,2} - k_{G,3} + k_{G,4}), \quad (\text{S29})$$

where the four components  $k_{G,i}$  ( $i = 1, 2, 3, 4$ ) are defined as

$$\begin{aligned} k_{G,1} &= \frac{4|\gamma_c|^2}{\epsilon^2 - \omega^2} \left( 4\omega^2\kappa - \frac{2\epsilon^2\kappa^2}{\kappa + 2\sqrt{\epsilon^2 - \omega^2}} - \frac{2\epsilon^2\kappa^2}{\kappa - 2\sqrt{\epsilon^2 - \omega^2}} \right) \Lambda_1^2 \\ &\quad + \frac{4|\gamma_c|^2}{\epsilon^2 - \omega^2} \left( 2\omega^2 - \frac{\epsilon^2\kappa}{\kappa + 2\sqrt{\epsilon^2 - \omega^2}} - \frac{\epsilon^2\kappa}{\kappa - 2\sqrt{\epsilon^2 - \omega^2}} \right) \Lambda_1 \\ &\quad + \frac{4|\gamma_c|^2}{\epsilon^2 - \omega^2} \left( 2\omega^2\kappa - \frac{\epsilon^2\kappa^2}{\kappa + 2\sqrt{\epsilon^2 - \omega^2}} - \frac{\epsilon^2\kappa^2}{\kappa - 2\sqrt{\epsilon^2 - \omega^2}} \right) |\Lambda_2|^2, \\ k_{G,2} &= \frac{4\omega\epsilon\kappa|\gamma_c|^2}{\epsilon^2 - \omega^2} \left( 6 - \frac{3\kappa}{\kappa + 2\sqrt{\epsilon^2 - \omega^2}} - \frac{3\kappa}{\kappa - 2\sqrt{\epsilon^2 - \omega^2}} \right) \Lambda_1 \text{Re}[\gamma_c\Lambda_2] \\ &\quad + \frac{4\omega\epsilon\kappa}{\epsilon^2 - \omega^2} \left( 2 - \frac{\kappa}{\kappa + 2\sqrt{\epsilon^2 - \omega^2}} - \frac{\kappa}{\kappa - 2\sqrt{\epsilon^2 - \omega^2}} \right) \text{Re}[\gamma_c\Lambda_2], \\ k_{G,3} &= -\frac{12\epsilon\kappa^2|\gamma_c|^2}{\sqrt{\epsilon^2 - \omega^2}} \left( \frac{1}{\kappa + 2\sqrt{\epsilon^2 - \omega^2}} - \frac{1}{\kappa - 2\sqrt{\epsilon^2 - \omega^2}} \right) \Lambda_1 \text{Im}[\gamma_c\Lambda_2] \\ &\quad - \frac{4\epsilon\kappa}{\sqrt{\epsilon^2 - \omega^2}} \left( \frac{1}{\kappa + 2\sqrt{\epsilon^2 - \omega^2}} - \frac{1}{\kappa - 2\sqrt{\epsilon^2 - \omega^2}} \right) \text{Im}[\gamma_c\Lambda_2] \\ &\quad + \frac{4\epsilon^2|\gamma_c|^2}{\sqrt{\epsilon^2 - \omega^2}} \left( \frac{1}{\kappa + 2\sqrt{\epsilon^2 - \omega^2}} - \frac{1}{\kappa - 2\sqrt{\epsilon^2 - \omega^2}} \right) (\Lambda_1 - \kappa\Lambda_3) \\ &\quad - \frac{4\epsilon^2\kappa|\gamma_c|^2}{\sqrt{\epsilon^2 - \omega^2}} \left( \frac{1}{(\kappa + 2\sqrt{\epsilon^2 - \omega^2})^2} - \frac{1}{(\kappa - 2\sqrt{\epsilon^2 - \omega^2})^2} \right) \Lambda_1 \\ k_{G,4} &= -8\kappa|\gamma_c|^4 (\Lambda_1 - \kappa\Lambda_3)\Lambda_1. \end{aligned} \quad (\text{S30})$$

Here, we have introduced the variables  $\Lambda_i$  ( $i = 1, 2, 3$ ), defined as

$$\begin{aligned} \Lambda_1 &= \frac{1}{2\text{Re}\lambda_-} + \frac{1}{2\text{Re}\lambda_+} - \frac{1}{\lambda_- + \lambda_+^*} - \frac{1}{\lambda_-^* + \lambda_+}, \\ \Lambda_2 &= \frac{\alpha_c}{2\lambda_-} - \frac{\beta_c}{2\lambda_+} - \frac{\alpha_c - \beta_c}{\lambda_- + \lambda_+}, \\ \Lambda_3 &= \frac{1}{4(\text{Re}\lambda_-)^2} + \frac{1}{4(\text{Re}\lambda_+)^2} - \frac{1}{(\lambda_- + \lambda_+^*)^2} - \frac{1}{(\lambda_-^* + \lambda_+)^2}. \end{aligned} \quad (\text{S31})$$

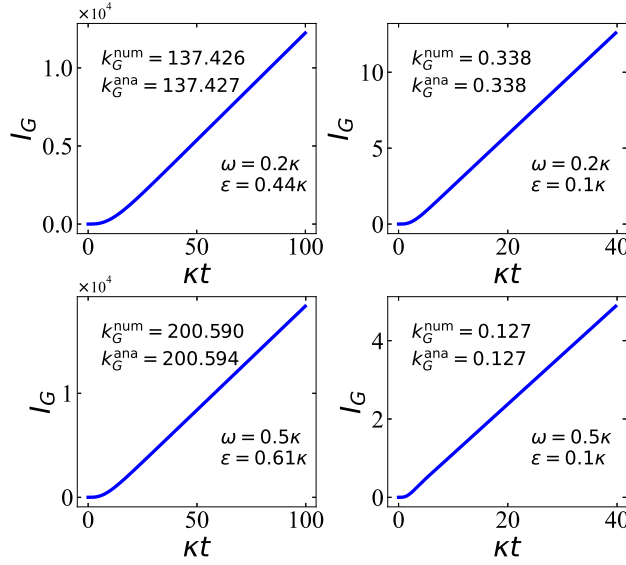


FIG. S5. The global QFI  $I_G$  (curves) calculated by numerically integrating Eq. (8) to compute the quantum fidelity  $\mathcal{F}(\omega_1, \omega_2)$ , and then evaluating the derivatives in Eq. (7) using finite difference. The corresponding long-time growth rates, denoted by  $k_G^{\text{num}}$ , are compared to the analytical results  $k_G^{\text{ana}}$  from Eq. (S29) for different choices of  $\omega$  and  $\epsilon$ .

## 2. Numerical justification

Here we provide numerical results to validate the analytical solution of  $k_G$  in Eq. (S29). Fig. S5 shows the time evolution of the global QFI  $I_G$  for randomly selected values of  $\omega$  and  $\epsilon$ . These curves are generated by numerically integrating Eq. (8) to compute the quantum fidelity  $\mathcal{F}(\omega_1, \omega_2)$ , and then evaluating the derivatives in Eq. (7) by means of finite difference. We perform a linear fit of these curves after they reach the linear regime to extract their slope  $k_G^{\text{num}}$ . These numerical fitted growth rates are in perfect agreement with the analytical results  $k_G^{\text{ana}}$  obtained from Eq. (S29) in all cases considered.

## C. Solutions for the moments of the unconditional state

Here we solve the unconditional open KPO model in the limit  $\chi \rightarrow 0$  using the Langevin approach. This method accounts for a Markovian environment in terms of the quantum white noise  $b(t)$ , which satisfies  $[b(t), b^\dagger(t')] = \delta(t-t')$ . We define the vectors  $\mathbf{a}(t) = (a(t), a^\dagger(t))^\top$  and  $\mathbf{b}(t) = (b(t), b^\dagger(t))^\top$ , and use the Heisenberg equation of motion to obtain

$$\frac{d\mathbf{a}(t)}{dt} = -\mathbf{A}_0\mathbf{a}(t) - \sqrt{\kappa}\mathbf{b}(t), \quad (\text{S32})$$

where the coefficient matrix  $\mathbf{A}_0$  is

$$\mathbf{A}_0 = \begin{pmatrix} i\omega + \kappa & i\epsilon \\ -i\epsilon & -i\omega + \kappa \end{pmatrix}. \quad (\text{S33})$$

Recalling that the initial state of the KPO is chosen as its vacuum, Eq. (S32) can then be integrated to yield the solution

$$a(t) = c_1(t)a(0) + c_2(t)a^\dagger(0) - \sqrt{\kappa} \int_0^t d\tau c_1(t-\tau)b(\tau) - \sqrt{\kappa} \int_0^t d\tau c_2(t-\tau)b^\dagger(\tau), \quad (\text{S34})$$

where the two coefficients are  $c_1(t) = \alpha_c e^{-\lambda-t} + \beta_c e^{-\lambda+t}$  and  $c_2(t) = \gamma_c (e^{-\lambda-t} - e^{-\lambda+t})$  with

$$\lambda_{\pm} = \kappa/2 \pm \sqrt{\epsilon^2 - \omega^2}, \quad \alpha_c = \frac{1}{2} - \frac{i\omega}{2\sqrt{\epsilon^2 - \omega^2}}, \quad \beta_c = \frac{1}{2} + \frac{i\omega}{2\sqrt{\epsilon^2 - \omega^2}}, \quad \gamma_c = \frac{-i\epsilon}{2\sqrt{\epsilon^2 - \omega^2}}. \quad (\text{S35})$$



Here,  $\lambda_{\pm}$  are the eigenvalues of the matrix  $\mathbf{A}_0$ .

Using the solution of  $a(t)$  in Eq. (S34), it is straightforward to find the explicit expressions of the moments  $\langle a^\dagger a \rangle_\mu$ ,  $\langle a^2 \rangle_\mu$ ,

$$\begin{aligned} \langle a^\dagger a \rangle_\mu(t) &= |\gamma_c|^2 \left( e^{-2\text{Re}\lambda_- t} + e^{-2\text{Re}\lambda_+ t} - 2\text{Re} e^{-(\lambda_- + \lambda_+^*)t} \right) + \kappa |\gamma_c|^2 \left( \frac{1 - e^{-2\text{Re}\lambda_- t}}{2\text{Re}\lambda_-} + \frac{1 - e^{-2\text{Re}\lambda_+ t}}{2\text{Re}\lambda_+} \right. \\ &\quad \left. - \frac{1 - e^{-(\lambda_- + \lambda_+^*)t}}{\lambda_- + \lambda_+^*} - \frac{1 - e^{-(\lambda_-^* + \lambda_+ )t}}{\lambda_-^* + \lambda_+} \right), \\ \langle a^2 \rangle_\mu(t) &= \gamma_c \left( \alpha_c e^{-2\lambda_- t} - \beta_c e^{-2\lambda_+ t} - (\alpha_c - \beta_c) e^{-(\lambda_- + \lambda_+ )t} \right) + \kappa \gamma_c \left( \alpha_c \frac{1 - e^{-2\lambda_- t}}{2\lambda_-} - \beta_c \frac{1 - e^{-2\lambda_+ t}}{2\lambda_+} \right. \\ &\quad \left. - (\alpha_c - \beta_c) \frac{1 - e^{-(\lambda_- + \lambda_+ )t}}{\lambda_- + \lambda_+} \right). \end{aligned} \quad (\text{S36})$$

On the other hand, using Wick's theorem the higher-order moments  $\langle a^{\dagger 3} a \rangle_\mu$  and  $\langle a^\dagger a^3 \rangle_\mu$  can be factorized as

$$\begin{aligned} \langle (a^\dagger a)^2 \rangle_\mu &= 2\langle a^\dagger a \rangle_\mu^2 + \langle a^\dagger a \rangle_\mu + \langle a^{\dagger 2} \rangle_\mu \langle a^2 \rangle_\mu - 2\langle a^\dagger \rangle_\mu^2 \langle a \rangle_\mu^2, \\ \langle a^{\dagger 3} a \rangle_\mu(t) &= 3\langle a^\dagger a \rangle_\mu \langle a^{\dagger 2} \rangle_\mu - 2\langle a^\dagger \rangle_\mu^3 \langle a \rangle_\mu, \quad \langle a^\dagger a^3 \rangle_\mu(t) = 3\langle a^\dagger a \rangle_\mu \langle a^2 \rangle_\mu - 2\langle a^\dagger \rangle_\mu \langle a \rangle_\mu^3. \end{aligned} \quad (\text{S37})$$

Consequently, all the moments with respect to the operator  $\mu$  appeared in Eq. (S19) can be derived using Eqs. (S36) and (S37). We close this subsection by presenting the explicit expressions for the components of  $\mathbf{f}(t)$  in Eq. (S22),

$$\begin{aligned} f_1 &= 2|\gamma_c|^4 \left( e^{-2\text{Re}\lambda_- t} + e^{-2\text{Re}\lambda_+ t} - 2\text{Re} e^{-(\lambda_- + \lambda_+^*)t} \right)^2 + 2\kappa^2 |\gamma_c|^4 \left( \frac{1 - e^{-2\text{Re}\lambda_- t}}{2\text{Re}\lambda_-} + \frac{1 - e^{-2\text{Re}\lambda_+ t}}{2\text{Re}\lambda_+} \right. \\ &\quad \left. - \frac{1 - e^{-(\lambda_- + \lambda_+^*)t}}{\lambda_- + \lambda_+^*} - \frac{1 - e^{-(\lambda_-^* + \lambda_+ )t}}{\lambda_-^* + \lambda_+} \right)^2 + 4\kappa |\gamma_c|^4 \left( e^{-2\text{Re}\lambda_- t} + e^{-2\text{Re}\lambda_+ t} - 2\text{Re} e^{-(\lambda_- + \lambda_+^*)t} \right) \\ &\quad \times \left( \frac{1 - e^{-2\text{Re}\lambda_- t}}{2\text{Re}\lambda_-} + \frac{1 - e^{-2\text{Re}\lambda_+ t}}{2\text{Re}\lambda_+} - \frac{1 - e^{-(\lambda_- + \lambda_+^*)t}}{\lambda_- + \lambda_+^*} - \frac{1 - e^{-(\lambda_-^* + \lambda_+ )t}}{\lambda_-^* + \lambda_+} \right) \\ &\quad + |\gamma_c|^2 \left( e^{-2\text{Re}\lambda_- t} + e^{-2\text{Re}\lambda_+ t} - 2\text{Re} e^{-(\lambda_- + \lambda_+^*)t} \right) + \kappa |\gamma_c|^2 \left( \frac{1 - e^{-2\text{Re}\lambda_- t}}{2\text{Re}\lambda_-} + \frac{1 - e^{-2\text{Re}\lambda_+ t}}{2\text{Re}\lambda_+} \right. \\ &\quad \left. - \frac{1 - e^{-(\lambda_- + \lambda_+^*)t}}{\lambda_- + \lambda_+^*} - \frac{1 - e^{-(\lambda_-^* + \lambda_+ )t}}{\lambda_-^* + \lambda_+} \right) + |\gamma_c|^2 \left| \alpha_c e^{-2\lambda_- t} - \beta_c e^{-2\lambda_+ t} - (\alpha_c - \beta_c) e^{-(\lambda_- + \lambda_+ )t} \right|^2 \\ &\quad + \kappa^2 |\gamma_c|^2 \left| \alpha_c \frac{1 - e^{-2\lambda_- t}}{2\lambda_-} - \beta_c \frac{1 - e^{-2\lambda_+ t}}{2\lambda_+} - (\alpha_c - \beta_c) \frac{1 - e^{-(\lambda_- + \lambda_+ )t}}{\lambda_- + \lambda_+} \right|^2 \\ &\quad + \kappa |\gamma_c|^2 \left( \alpha_c e^{-2\lambda_- t} - \beta_c e^{-2\lambda_+ t} - (\alpha_c - \beta_c) e^{-(\lambda_- + \lambda_+ )t} \right) \left( \alpha_c^* \frac{1 - e^{-2\lambda_-^* t}}{2\lambda_-^*} - \beta_c^* \frac{1 - e^{-2\lambda_+^* t}}{2\lambda_+^*} \right. \\ &\quad \left. - (\alpha_c^* - \beta_c^*) \frac{1 - e^{-(\lambda_-^* + \lambda_+^*)t}}{\lambda_-^* + \lambda_+^*} \right) + \kappa |\gamma_c|^2 \left( \alpha_c^* e^{-2\lambda_-^* t} - \beta_c^* e^{-2\lambda_+^* t} - (\alpha_c^* - \beta_c^*) e^{-(\lambda_-^* + \lambda_+^*)t} \right) \left( \alpha_c \frac{1 - e^{-2\lambda_- t}}{2\lambda_-} \right. \\ &\quad \left. - \beta_c \frac{1 - e^{-2\lambda_+ t}}{2\lambda_+} - (\alpha_c - \beta_c) \frac{1 - e^{-(\lambda_- + \lambda_+ )t}}{\lambda_- + \lambda_+} \right), \end{aligned} \quad (\text{S38})$$

$$\begin{aligned}
f_2 = & 3|\gamma_c|^2 \left( e^{-2\text{Re}\lambda_- t} + e^{-2\text{Re}\lambda_+ t} - 2\text{Re} e^{-(\lambda_- + \lambda_+^*)t} \right) \\
& \times \left[ \gamma_c \left( \alpha_c e^{-2\lambda_- t} - \beta_c e^{-2\lambda_+ t} - (\alpha_c - \beta_c) e^{-(\lambda_- + \lambda_+^*)t} \right) + \gamma_c^* \left( \alpha_c^* e^{-2\lambda_-^* t} - \beta_c^* e^{-2\lambda_+^* t} - (\alpha_c^* - \beta_c^*) e^{-(\lambda_-^* + \lambda_+^*)t} \right) \right] \\
& + 3\kappa |\gamma_c|^2 \left( \frac{1 - e^{-2\text{Re}\lambda_- t}}{2\text{Re}\lambda_-} + \frac{1 - e^{-2\text{Re}\lambda_+ t}}{2\text{Re}\lambda_+} - \frac{1 - e^{-(\lambda_- + \lambda_+^*)t}}{\lambda_- + \lambda_+^*} - \frac{1 - e^{-(\lambda_-^* + \lambda_+^*)t}}{\lambda_-^* + \lambda_+} \right) \\
& \times \left[ \gamma_c \left( \alpha_c e^{-2\lambda_- t} - \beta_c e^{-2\lambda_+ t} - (\alpha_c - \beta_c) e^{-(\lambda_- + \lambda_+^*)t} \right) + \gamma_c^* \left( \alpha_c^* e^{-2\lambda_-^* t} - \beta_c^* e^{-2\lambda_+^* t} - (\alpha_c^* - \beta_c^*) e^{-(\lambda_-^* + \lambda_+^*)t} \right) \right] \\
& + 3|\gamma_c|^2 \left( e^{-2\text{Re}\lambda_- t} + e^{-2\text{Re}\lambda_+ t} - 2\text{Re} e^{-(\lambda_- + \lambda_+^*)t} \right) \left[ \kappa \gamma_c \left( \alpha_c \frac{1 - e^{-2\lambda_- t}}{2\lambda_-} - \beta_c \frac{1 - e^{-2\lambda_+ t}}{2\lambda_+} \right. \right. \\
& \left. \left. - (\alpha_c - \beta_c) \frac{1 - e^{-(\lambda_- + \lambda_+^*)t}}{\lambda_- + \lambda_+^*} \right) + \kappa \gamma_c^* \left( \alpha_c^* \frac{1 - e^{-2\lambda_-^* t}}{2\lambda_-^*} - \beta_c^* \frac{1 - e^{-2\lambda_+^* t}}{2\lambda_+^*} - (\alpha_c^* - \beta_c^*) \frac{1 - e^{-(\lambda_-^* + \lambda_+^*)t}}{\lambda_-^* + \lambda_+} \right) \right] \\
& + 3\kappa |\gamma_c|^2 \left( \frac{1 - e^{-2\text{Re}\lambda_- t}}{2\text{Re}\lambda_-} + \frac{1 - e^{-2\text{Re}\lambda_+ t}}{2\text{Re}\lambda_+} - \frac{1 - e^{-(\lambda_- + \lambda_+^*)t}}{\lambda_- + \lambda_+^*} - \frac{1 - e^{-(\lambda_-^* + \lambda_+^*)t}}{\lambda_-^* + \lambda_+} \right) \left[ \kappa \gamma_c \left( \alpha_c \frac{1 - e^{-2\lambda_- t}}{2\lambda_-} \right. \right. \\
& \left. \left. - \beta_c \frac{1 - e^{-2\lambda_+ t}}{2\lambda_+} - (\alpha_c - \beta_c) \frac{1 - e^{-(\lambda_- + \lambda_+^*)t}}{\lambda_- + \lambda_+^*} \right) + \kappa \gamma_c^* \left( \alpha_c^* \frac{1 - e^{-2\lambda_-^* t}}{2\lambda_-^*} - \beta_c^* \frac{1 - e^{-2\lambda_+^* t}}{2\lambda_+^*} - (\alpha_c^* - \beta_c^*) \frac{1 - e^{-(\lambda_-^* + \lambda_+^*)t}}{\lambda_-^* + \lambda_+} \right) \right] \\
& + \gamma_c \left( \alpha_c e^{-2\lambda_- t} - \beta_c e^{-2\lambda_+ t} - (\alpha_c - \beta_c) e^{-(\lambda_- + \lambda_+^*)t} \right) + \gamma_c^* \left( \alpha_c^* e^{-2\lambda_-^* t} - \beta_c^* e^{-2\lambda_+^* t} - (\alpha_c^* - \beta_c^*) e^{-(\lambda_-^* + \lambda_+^*)t} \right) \\
& + \kappa \gamma_c \left( \alpha_c \frac{1 - e^{-2\lambda_- t}}{2\lambda_-} - \beta_c \frac{1 - e^{-2\lambda_+ t}}{2\lambda_+} - (\alpha_c - \beta_c) \frac{1 - e^{-(\lambda_- + \lambda_+^*)t}}{\lambda_- + \lambda_+^*} \right) \\
& + \kappa \gamma_c^* \left( \alpha_c^* \frac{1 - e^{-2\lambda_-^* t}}{2\lambda_-^*} - \beta_c^* \frac{1 - e^{-2\lambda_+^* t}}{2\lambda_+^*} - (\alpha_c^* - \beta_c^*) \frac{1 - e^{-(\lambda_-^* + \lambda_+^*)t}}{\lambda_-^* + \lambda_+} \right).
\end{aligned} \tag{S39}$$

$$\begin{aligned}
f_3 &= 3\langle a^\dagger a \rangle_{\bar{\rho}} \langle a^{\dagger 2} \rangle_{\bar{\rho}} - 3\langle a^\dagger a \rangle_{\bar{\rho}} \langle a^2 \rangle_{\bar{\rho}} + \langle a^{\dagger 2} \rangle_{\bar{\rho}} - \langle a^2 \rangle_{\bar{\rho}} + \epsilon \langle 1 \rangle_{\partial_{\delta\omega} \bar{\rho}} \\
&= 3|\gamma_c|^2 \left( e^{-2\text{Re}\lambda_- t} + e^{-2\text{Re}\lambda_+ t} - 2\text{Re} e^{-(\lambda_- + \lambda_+^*)t} \right) \\
&\quad \times \left[ -\gamma_c \left( \alpha_c e^{-2\lambda_- t} - \beta_c e^{-2\lambda_+ t} - (\alpha_c - \beta_c) e^{-(\lambda_- + \lambda_+ t)} \right) + \gamma_c^* \left( \alpha_c^* e^{-2\lambda_-^* t} - \beta_c^* e^{-2\lambda_+^* t} - (\alpha_c^* - \beta_c^*) e^{-(\lambda_-^* + \lambda_+^*)t} \right) \right] \\
&\quad + 3\kappa |\gamma_c|^2 \left( \frac{1 - e^{-2\text{Re}\lambda_- t}}{2\text{Re}\lambda_-} + \frac{1 - e^{-2\text{Re}\lambda_+ t}}{2\text{Re}\lambda_+} - \frac{1 - e^{-(\lambda_- + \lambda_+^*)t}}{\lambda_- + \lambda_+^*} - \frac{1 - e^{-(\lambda_-^* + \lambda_+ t)}}{\lambda_-^* + \lambda_+} \right) \\
&\quad \times \left[ -\gamma_c \left( \alpha_c e^{-2\lambda_- t} - \beta_c e^{-2\lambda_+ t} - (\alpha_c - \beta_c) e^{-(\lambda_- + \lambda_+ t)} \right) + \gamma_c^* \left( \alpha_c^* e^{-2\lambda_-^* t} - \beta_c^* e^{-2\lambda_+^* t} - (\alpha_c^* - \beta_c^*) e^{-(\lambda_-^* + \lambda_+^*)t} \right) \right] \\
&\quad + 3|\gamma_c|^2 \left( e^{-2\text{Re}\lambda_- t} + e^{-2\text{Re}\lambda_+ t} - 2\text{Re} e^{-(\lambda_- + \lambda_+^*)t} \right) \left[ -\kappa \gamma_c \left( \alpha_c \frac{1 - e^{-2\lambda_- t}}{2\lambda_-} - \beta_c \frac{1 - e^{-2\lambda_+ t}}{2\lambda_+} \right. \right. \\
&\quad \left. \left. - (\alpha_c - \beta_c) \frac{1 - e^{-(\lambda_- + \lambda_+ t)}}{\lambda_- + \lambda_+} \right) + \kappa \gamma_c^* \left( \alpha_c^* \frac{1 - e^{-2\lambda_-^* t}}{2\lambda_-^*} - \beta_c^* \frac{1 - e^{-2\lambda_+^* t}}{2\lambda_+^*} - (\alpha_c^* - \beta_c^*) \frac{1 - e^{-(\lambda_-^* + \lambda_+^*)t}}{\lambda_-^* + \lambda_+^*} \right) \right] \\
&\quad + 3\kappa |\gamma_c|^2 \left( \frac{1 - e^{-2\text{Re}\lambda_- t}}{2\text{Re}\lambda_-} + \frac{1 - e^{-2\text{Re}\lambda_+ t}}{2\text{Re}\lambda_+} - \frac{1 - e^{-(\lambda_- + \lambda_+^*)t}}{\lambda_- + \lambda_+^*} - \frac{1 - e^{-(\lambda_-^* + \lambda_+ t)}}{\lambda_-^* + \lambda_+} \right) \left[ -\kappa \gamma_c \left( \alpha_c \frac{1 - e^{-2\lambda_- t}}{2\lambda_-} \right. \right. \\
&\quad \left. \left. - \beta_c \frac{1 - e^{-2\lambda_+ t}}{2\lambda_+} - (\alpha_c - \beta_c) \frac{1 - e^{-(\lambda_- + \lambda_+ t)}}{\lambda_- + \lambda_+} \right) + \kappa \gamma_c^* \left( \alpha_c^* \frac{1 - e^{-2\lambda_-^* t}}{2\lambda_-^*} - \beta_c^* \frac{1 - e^{-2\lambda_+^* t}}{2\lambda_+^*} - (\alpha_c^* - \beta_c^*) \frac{1 - e^{-(\lambda_-^* + \lambda_+^*)t}}{\lambda_-^* + \lambda_+^*} \right) \right] \\
&\quad - \gamma_c \left( \alpha_c e^{-2\lambda_- t} - \beta_c e^{-2\lambda_+ t} - (\alpha_c - \beta_c) e^{-(\lambda_- + \lambda_+ t)} \right) + \gamma_c^* \left( \alpha_c^* e^{-2\lambda_-^* t} - \beta_c^* e^{-2\lambda_+^* t} - (\alpha_c^* - \beta_c^*) e^{-(\lambda_-^* + \lambda_+^*)t} \right) \\
&\quad - \kappa \gamma_c \left( \alpha_c \frac{1 - e^{-2\lambda_- t}}{2\lambda_-} - \beta_c \frac{1 - e^{-2\lambda_+ t}}{2\lambda_+} - (\alpha_c - \beta_c) \frac{1 - e^{-(\lambda_- + \lambda_+ t)}}{\lambda_- + \lambda_+} \right) \\
&\quad + \kappa \gamma_c^* \left( \alpha_c^* \frac{1 - e^{-2\lambda_-^* t}}{2\lambda_-^*} - \beta_c^* \frac{1 - e^{-2\lambda_+^* t}}{2\lambda_+^*} - (\alpha_c^* - \beta_c^*) \frac{1 - e^{-(\lambda_-^* + \lambda_+^*)t}}{\lambda_-^* + \lambda_+^*} \right) \\
&\quad + 2i\epsilon |\gamma_c|^2 \left( \frac{1 - e^{-2\text{Re}\lambda_- t}}{2\text{Re}\lambda_-} + \frac{1 - e^{-2\text{Re}\lambda_+ t}}{2\text{Re}\lambda_+} - 2\text{Re} \frac{1 - e^{-(\lambda_- + \lambda_+^*)t}}{\lambda_- + \lambda_+^*} \right) + 2i\epsilon \kappa |\gamma_c|^2 \left( \frac{2\text{Re}\lambda_- t - 1 + e^{-2\text{Re}\lambda_- t}}{4\text{Re}^2\lambda_-} \right. \\
&\quad \left. + \frac{2\text{Re}\lambda_+ t - 1 + e^{-2\text{Re}\lambda_+ t}}{4\text{Re}^2\lambda_+} - \frac{(\lambda_- + \lambda_+^*)t - 1 + e^{-(\lambda_- + \lambda_+^*)t}}{(\lambda_- + \lambda_+^*)^2} - \frac{(\lambda_-^* + \lambda_+)t - 1 + e^{-(\lambda_-^* + \lambda_+)t}}{(\lambda_-^* + \lambda_+)^2} \right)
\end{aligned} \tag{S40}$$